Spring 2017

Designer Metasurfaces for On Demand Optical Responses

Matthew S. LePain

Recommended Citation

LePain, Matthew S., "Designer Metasurfaces for On Demand Optical Responses" (2017). *Electronic Theses and Dissertations*. 1558.
https://digitalcommons.georgiasouthern.edu/etd/1558

DESIGNER METASURFACES FOR ON DEMAND OPTICAL RESPONSES

by

MATTHEW S. LEPAIN

(Under the Direction of Maxim Durach)

ABSTRACT

Nanostructured materials are one of the leading areas in photonics currently. These structures offer almost limitless possibilities in the manipulation of light. Using two different semi-analytical simulation methods, I show a few of the possible properties that these nanostructures possess, including polarization rotation and coupling with electronics.

INDEX WORDS: Nanotechnology, Plasmon, Metamaterial, Wave plate, Polarization, Photonics

DESIGNER METASURFACES FOR ON DEMAND OPTICAL RESPONSES

by

MATTHEW S. LEPAIN

B.S., Georgia Southern University, 2014

A Thesis Submitted to the Graduate Faculty of Georgia Southern University in Partial Fulfillment of the Requirements for the Degree

MASTER OF SCIENCE

STATESBORO, GEORGIA

DESIGNER METASURFACES FOR ON DEMAND OPTICAL RESPONSES

by

MATTHEW S. LEPAIN

Major Professor:	Maxim Durach
Committee:	Clayton Heller Li Ma

Electronic Version Approved:

May 2017

TABLE OF CONTENTS

Page

LIST OF FIGURES

Page

Chapter 1

Introduction

The goal of this work is to demonstrate that metal-dielectric metasurfaces can exhibit a broad range of optical, optoelectronic and even mechanical responses to optical excitation. To do this I used theoretical and computational approaches of wave optics on the subwavelength and wavelength scales. At the wavelength scale structures tend to exhibit strong coupling between surface plasmon polaritons (SPPs) and far field waves via diffraction while on subwavelength scales diffraction is suppressed and structural features act similarly to atoms leading to what is called metamaterials. Using these properties we have shown that one can have full control over the polarization of light, photoinduced currents, and reflectivity of metasurfaces.

The first subject to be introduced is plasmonics, the study of plasmons, or density waves in the sea of electrons present in metals. Historically, one of the first dives into this subject was via what is now known as Mie theory[1], in which Dr. Gustav Mie, in attempting to explain the color of gold nanospheres, considered a simple spherical object. He was able to solve the electrodynamic problem, but did not go as far as to introducing the plasmons as density waves in metal plasma. That distinction goes to David Bohm and David Pines who wished to model the reactions of electrons in a metal to external oscillating electric fields using quantum mechanics[2-5]. In this endeavor, they quickly found that mapping each electron was utterly infeasible, instead adopting the idea of them acting as one entity, a dense electron plasma. Finding that this model was still insufficient, they added electron-electron interaction perturbations into the Hamiltonian finally leading to the understanding that is still used today. From a macroscopic electrodynamics point of view, main requirement for plasmons is negative dielectric permittivity of one of the material, which is characteristic of metals.

Nowadays, it is well understood how to excite plasmons. One of the simplest methods is to fire electrons at the surface of a metal. R. H. Ritchie was the first to introduce this method in a technique which is called electron energy loss spectroscopy (EELS) [6]. The next method involves the use of high index of refraction materials used as prisms, with metal structures deposited on one side of the prism. This way plasmons can be excited at the metal structures using what is called Otto [7] and Kretschmann [8] geometries. Plasmons can also be excited in metal nanostructures by diffraction. In periodic nanostructures, such as grating structures plasmons appear if a diffraction order k-vector $k_n = k_{ins} + \frac{2\pi n}{d}$ matches the k-vector of a plasmon k_{SPP}.

The beauty and expanse of the field of photonics stems from the fact that even within a linear optics approximation, consideration of different shapes and material properties of various structures leads to complexity, which has never been fully explored. If one considers a generic structure for which electromagnetic fields need to be found, there are two ways to approach this problem. The first one, which has been actively utilized in commercial software, is to solve Maxwell equations on a grid. There are disadvantages of this approach, in particular, that this approach is purely numerical leaving no space for analytical analysis. Another disadvantage stems from possible disparity between scales of wavelength and geometrical sizes when computing fields in nanostructures, leading to prohibitive computational costs.

Another way to find a solution of Maxwell equations in a generic structure is to represent fields in each region of homogeneity as an expansion over a suitable basis of solutions and then find the expansion coefficients from boundary conditions. In Cartesian coordinates the basis of choice is complex exponentials with dispersion:

$$\frac{\omega^2}{\mu\epsilon} = \boldsymbol{k}^2, \tag{1.1}$$

where ω is frequency, μ represents the media's magnetic response, and ϵ its electric, and $\mathbf{k}$ is the k-vector. This allows for two types of waves, plain waves in the far field, where all the components of $\mathbf{k}$ are real, and evanescent in the near field, where a component of $\mathbf{k}$ is imaginary. This method applied to a single planar boundary between materials leads to the well-known Fresnel equations, originally deduced by Augustin-Jean Fresnel in 1823 [9]. Adding a second boundary turns a structure into a Fabry-Pérot cavity, first considered by Airy [10]. Airy's solution is very important since it allows for the description of multiple realistic experimental geometries, including planar dielectric waveguides, metal-insulator-metal (MIM) structures and plasmon excitation in Kretschmann geometry. This can be generalized to multiple boundaries by using the transfer matrix method, which allows for efficient solutions of fields and reflection and transmission coefficients for multilayered structures, such as distributed Bragg reflectors (DBR) or parallel-plate metamaterials. This can even be taken one step further to an infinite set of layers, if these layers repeat periodically, then the boundary conditions can be reduced to a single Kronig-Penney equation. This effectively leads to a new material, which on wavelength scale is called a photonic crystal, and on subwavelength scale is an anisotropic metamaterial.

The structures composed of parallel layers with planar boundaries are very important and describe a lot of important practical situation, but in many cases it is interesting to consider more generic structures. But what can be done analytically or semi-analytically that isn't just a simple set of parallel layers? One might consider taking plane-wave solutions and matching them on non-planar boundaries. At first one might think this impossible - how could a plane wave match a different plane wave on any boundary other than a plane? One can argue that, due to the translational symmetry of the system in the directions of periodicity, if one moves one period along the surface and gain a complex phase ϕ in the incident field, any wave that produces the same complex phase shift may be produced by the structure, and no others. This reduces the number of possible plane waves from $|\mathbb{R}|$ to $\aleph_0$. While still technically impossible to analytically solve, the problem becomes more tractable.

To be specific, consider a boundary between 2 materials with an arbitrary periodic profile. One can assume that the field in both materials can be described as corresponding sets of diffraction waves, which is called Rayleigh approximation [11]. This approach is frequently used, nevertheless as was shown in Ref. [12] that this method has an upper limit on height for any given structure. And Millar [13, 14] showed that for a sine wave profile boundary $f(x) = b\sin(\kappa x)$, that method only works for $b\kappa < 0.448$.

In 1982 a vastly different approach was attempted by J. Chandezon [15]. In his method, instead of extending the diffraction-wave expansion into the region of the gratings, new basis waves, dependent on the details of the boundary profile, are constructed in a modified coordinate system where the structure's surface is flat. The expansion coefficients are then found from matching these waves at the flat interface in the transformed coordinates. I describe this method in details in Chapter 4. One of the problems of this method, which I encountered during my work, is that in structures with steep profiles the convergence is hard to achieve and taking into account many diffraction waves is required.

In Chapters 3 and 5 I describe the major results achieved. In 3 it is shown that with small periods the structure described in Chapter 2 forms a metamaterial layer and can act as a wave plate over as small a distance as 30 nm. We described the optical spectrum of this metasurface for the first time to our knowledge. The array of nanowires can serve as an anisotropic metasurface with epsilon-near-pole and epsilon-near-zero responses along different axes of the structure. Chapter 5 touches on how a sine wave structure can be used to generate electrical currents for potential use in optoelectronic devices. We also compare optical properties of the sine-wave and square-grating metasurfaces with the same period and show that they support the same SPP spectrum, but exhibit entirely opposite optical power distribution over reflection and transmission channels.

Chapter 2

New Method for Calculation of Optical Properties in Square-Grating Metasurfaces

Modern nanotechnology poses a plethora of cutting-edge research problems in the fields of nano-optics and electronics, which are ideal for reinforcement of the knowledge gained in the upper division physics courses, such as Classical Electromagnetics and Quantum Mechanics, as well as for training in numerical methods and computational techniques. Due to exquisite spatial profile of nanostructures, the solutions to these problems feature combinations of propagating and evanescent waves. This is known to pose considerable numerical complications if care is not taken. In particular, applying the straightforward routine of setting boundary conditions at nanostructure boundaries results in poorly conditioned systems of equations and unacceptable errors due to evanescent waves. This has been discussed for a number of optical structures, including stratified media [16], and sine-wave grating [17].

Plasmonic metamaterials and metasurfaces is a rapidly developing field, which encompasses such phenomena as negative refraction [18], superlensing [19], optical cloaking [20], wavefront control [21] and much more. Plasmons are evanescent waves bound to the interfaces between metal and dielectric materials. The new functionalities are achieved when metal-dielectric structures feature subwavelength design forming metamaterials. The bright modes of these structures behave according to the effective metamaterial medium approximation, whereas the dark plasmonic modes are strongly localized. This leads to the numerical issues related to presence of both propagating and evanescent fields to be strongly expressed in metamaterial structures.

In this Chapter, we present a comparison of two techniques to calculate electromagnetic fields in a nanostructure, which contains an array of nanoscale metal plates separated by layers of high-index dielectric placed above a transparent substrate. This problem is very important for the fields of photonics and metamaterials and its solution will allow the modeling of ultra-thin polarization rotators and nanoscale light emitters with controlled polarization [22].

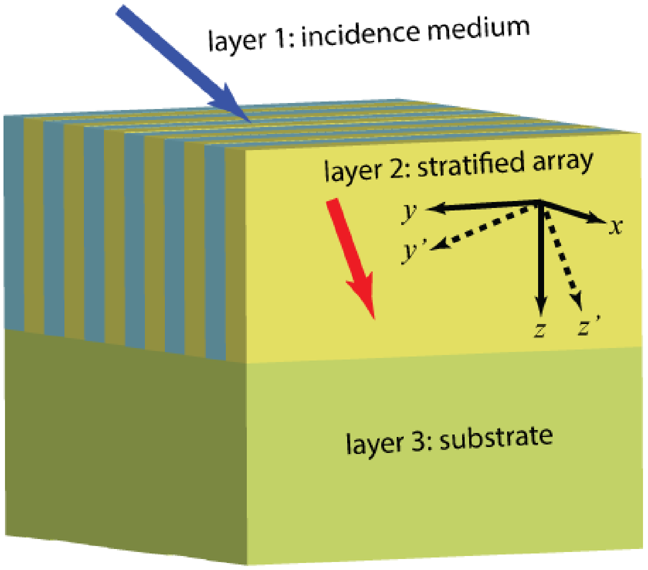

Fig. 2.1: Structure Schematics. The three-layer structure considered in this chapter contains a one-dimensional metamaterial in layer 2. Note that the selection of coordinates that are shown here are explained in the text.

From the computational perspective this structure requires simultaneous consideration of propagating and evanescent waves, therefore the boundary condition equations are numerically unstable [16, 17]. We devise a transfer matrix computational technique specific to this structure to resolve this issue by dynamically removing the evanescent waves from the computation as they decay in the structure.

Methods

Consider a three-layered structure composed of layers 1 and 3, which are homogeneous and isotropic and layer 2, which is a one dimensionally periodic array of two different homogeneous and isotropic materials (Fig. 2.1). Because of the periodicity of layer 2 diffraction waves will be produced in layers 1 and 3 with diffraction wave vectors

$$k_x^{(n)} = k_x + \frac{2\pi n}{d} \tag{2.1}$$

Here d is the period of the structure. The fields in layer 1 will be represented as:

$$\boldsymbol{F} = Re\left[e^{i\omega t}\left(I\, e^{i\boldsymbol{k_0}\cdot\boldsymbol{r}} + \sum_{n=-\infty}^{\infty} R_n\, e^{-i\boldsymbol{k_n}\cdot\boldsymbol{r}}\right)\right]\hat{\boldsymbol{f}} \tag{2.2}$$

where F is either the magnetic field H (for TM polarization) or the electric field E (TE polarization) and $\hat{\boldsymbol{f}}$ is in the transverse direction. The R_ns are amplitudes of the reflected waves, and $I = P$ for TM fields and $I = S$ for TE fields is the incident wave amplitude. Also ω is the angular frequency, $\boldsymbol{k_0} = k_x\hat{\boldsymbol{x}} + k_y\hat{\boldsymbol{y}} + k_z\hat{\boldsymbol{z}}$, $\boldsymbol{r}$ is the position vector, and $\boldsymbol{k_n} = k_x^{(n)}\hat{\boldsymbol{x}} + k_y\hat{\boldsymbol{y}} + \sqrt{k_0^2\varepsilon_I - {k_x^{(n)}}^2 - k_y^2}\,\hat{\boldsymbol{z}}$. In layer 3 the fields are represented as:

$$\boldsymbol{F} = Re\left[e^{i\omega t}\sum_{n=-\infty}^{\infty} T_n\, e^{i\boldsymbol{k_n}\cdot\boldsymbol{r}}\right]\hat{\boldsymbol{f}} \tag{2.3}$$

Where the T_ns are amplitudes of transmitted waves.

The fields in layer 2 are more complicated. Because of the reflections on the layers' boundaries, waves that propagate in the positive and negative *x* directions are present in each material. In the case that the incidence plane is at an angle to the stratification of layer 2 (*x* direction), the convenient directions in which to define polarization are different within each layer. This leads to the fields being excessively complicated to solve in the *x*-*y*-*z* coordinate system. Thus, we simply consider a wave propagating in the z' direction and rotate the coordinates back when convenient (see Fig. 2.1). The un-rotated field equations look like this:

$$F_{y'}^{(m)} = Re\left[e^{i\omega t}\left(A_m e^{ik_{z'}^{(m)}z'} + B_m e^{-ik_{z'}^{(m)}z'}\right)\times\begin{cases}C_m e^{i\alpha_1 x} + D_m e^{-i\alpha_1 x} & Material\ 1\\ G_m e^{i\alpha_2 x} + J_m e^{-i\alpha_2 x} & Material\ 2\end{cases}\right] \tag{2.4}$$

A_m, B_m, C_m, D_m, G_m, and J_m are unknown amplitudes, and $\alpha_n = \sqrt{k_0^2\varepsilon_n - k_{z'}^{(m)^2}}$.

This equation alone has in it 7 unknowns. Fortunately A_m and B_m can be found via the upper and lower boundary conditions, but C_m, D_m, G_m, J_m, and $k_{z'}^{(m)}$ must be solved for. To do this we must use Maxwell's equations and the boundary conditions for *E* and *H* fields at metal/dielectric boundaries. For *p* polarization ($\boldsymbol{F} \rightarrow \boldsymbol{H}$):

$$E_x = \frac{k_{z'}^{(m)}}{k_0\varepsilon}H_{y'} \tag{2.5}$$

$$E_{z'} = \frac{i}{k_0\varepsilon}\frac{\partial H_{y'}}{\partial x} \tag{2.6}$$

The field components $H_{y'}$ and $E_{z'}$ are continuous across the boundary therefore:

$$C_m e^{i\alpha_1 d_1} + D_m e^{-i\alpha_1 d_1} = G_m + J_m \tag{2.7}$$

$$\frac{\alpha_1}{k_0\varepsilon_1}\left(C_m e^{i\alpha_1 d_1} - D_m e^{-i\alpha_1 d_1}\right) = \frac{\alpha_2}{k_0\varepsilon_2}(G_m - J_m) \tag{2.8}$$

Here d_1 is the width of the first layer. In matching the period boundary we must take into account the phase factor $e^{ik_x d}$ in order to be able to match the phase in layers 1 and 3 to this one. This leads to the equations

$$(C_m + D_m)e^{ik_x d} = G_m e^{i\alpha_2 d_2} + J_m e^{-i\alpha_2 d_2} \tag{2.9}$$

$$\frac{\alpha_1}{k_0\varepsilon_1}(C_m - D_m)e^{ik_x d} = \frac{\alpha_2}{k_0\varepsilon_2}\left(G_m e^{i\alpha_2 d_2} - J_m e^{-i\alpha_2 d_2}\right) \tag{2.10}$$

Where d_2 is the width of the second layer.

These four boundary conditions result in the Kronig-Penny (KP) equation:

$$\cos \alpha_1 d_1 \cos \alpha_2 d_2 - \frac{1}{2}\left(\frac{p_1}{p_2} + \frac{p_2}{p_1}\right) \sin \alpha_1 d_1 \sin \alpha_2 d_2 = \cos k_x d \tag{2.11}$$

with $p_i = \frac{\alpha_i}{k_0 \varepsilon_i}$. For s polarization ($\boldsymbol{F} \to \boldsymbol{E}$) the characteristic equation is similar, except that $p_i = -\frac{\alpha_i}{k_0}$.

The KP equation provides the means to find $k_{z'}^{(m)}$ and the corresponding C_m, D_m, G_m, and J_m coefficients. Unfortunately, the KP equation is transcendental and has an infinite number of roots. It is however quite possible to find a finite set of roots for an individual set of parameters[23, 24]. But to get any directly relatable data we need to be able to look at a wide swath of the parameter space with good resolution simultaneously.

The process to find roots for a single set of parameters is to first choose a maximum value for $\left|k_{z'}^{(m)}\right|$, this gives a minimum decay length and wavelength to be considered. Then we create a graph overlaying the zero contours of the real and imaginary parts of the KP equation as a function of the real and imaginary parts of ${k_{z'}^{(m)}}^2$ (see Fig. 2.2). The desired roots are at the intersections of these contours.

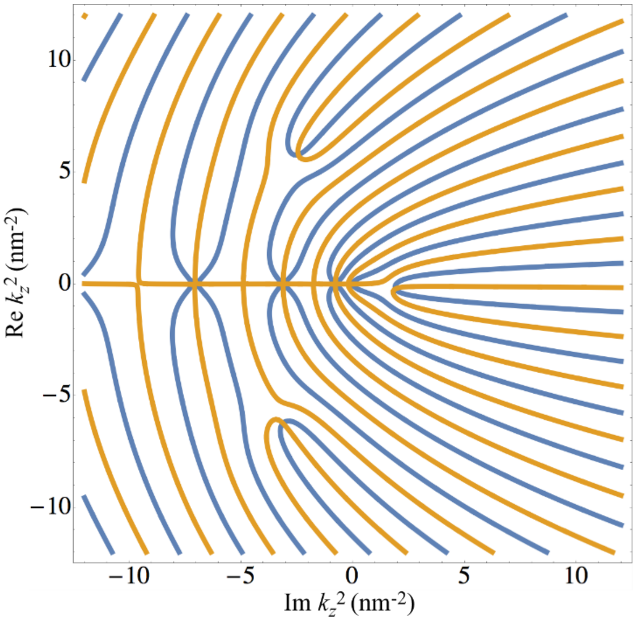

Fig. 2.2: A graph of the zero contour curves of the real (blue) and imaginary (orange) parts of the KP equation [Eq. (2.11)] using 8.5 nm GaAs and 1.5 nm Ag at $\omega = 2.47$ eV and normal incidence ($k_x = 0$).

To find the $k_{z'}^{(m)}$ in the desired range of parameters we use an iterative method in which we first do the above process for one set of parameters. Then we use those roots as the starting point for very slightly different parameters iterating until the whole parameter space is covered.

This process leads to roots jumping from one branch to another even as we reached the upper limit of a reasonable number of iterations. To avoid this we use a pair of equations that split the KP equation into even and odd roots as long as the angle of incidence is zero, in other words $k_x = 0$. [24]

$$p_1 \tan\left(\frac{p_2 d_2}{2}\right) + p_2 \tan\left(\frac{p_1 d_1}{2}\right) = 0 \tag{2.12}$$

$$p_2 \tan\left(\frac{p_2 d_2}{2}\right) + p_1 \tan\left(\frac{p_1 d_1}{2}\right) = 0 \tag{2.13}$$

These equations split all the troublesome roots apart into the two separate equations as visible in Fig. 2.3. However, there are still two roots of Eqn. (2.13) in p polarization that continue to have this issue. We have gotten around this issue by simultaneously changing multiple parameters in a single step such that the roots change much slower throughout the sections where the roots would normally need much higher resolution.

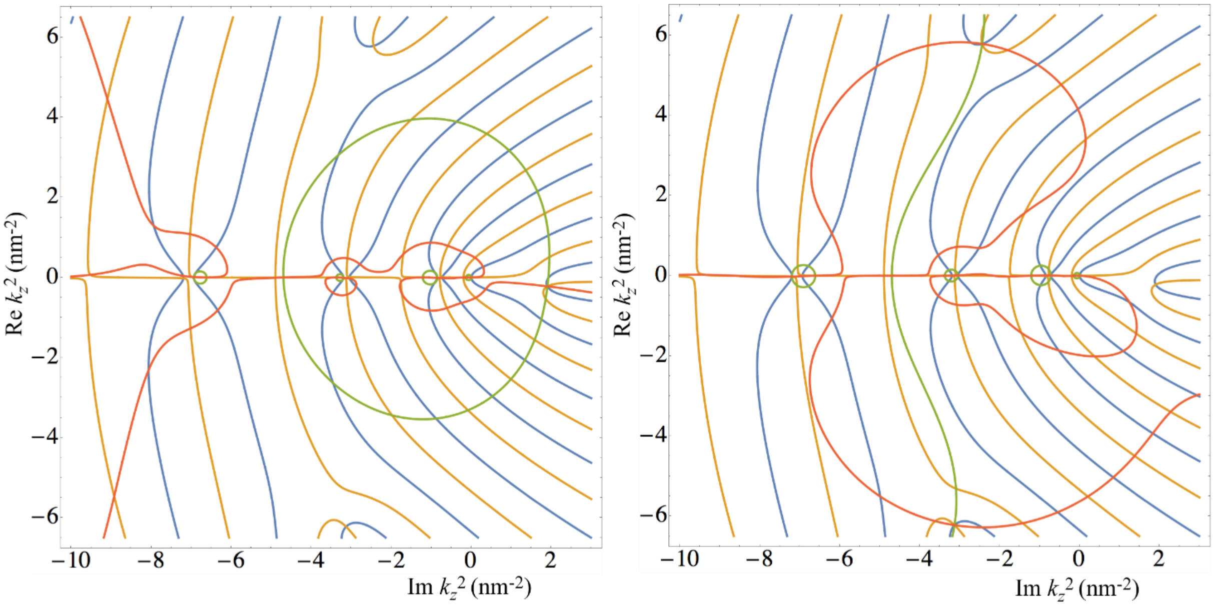

Fig. 2.3: A graph of the zero contour curves of the real (green) and imaginary (red) parts of the left sides of Eqs. (2.12) (left) and (2.13) (right) using the same parameters as Fig. 2.2 and overlaid on top of Fig. 2.2.

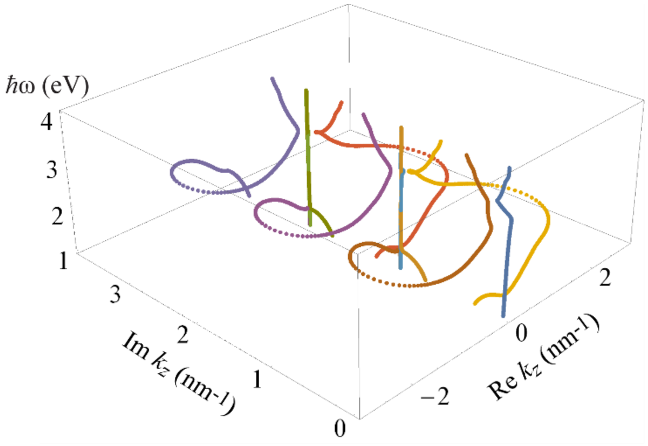

Fig. 2.4: Roots of the KP equation [Eq. (2.11)-(2.13)] as a function of frequency for 7.5 nm GaAs & 2.5 nm Ag, at normal incidence.

After the modes in layer 2 are found (see Fig. 2.4) the fields need to be matched at the upper and lower boundaries. First we need to identify all the independent waves that are present.

Table 1: The waves and their amplitudes within each layer

Layer 1	
TM Incident	P
TE Incident	S
TM Diffraction	R_{Mn}
TE Diffraction	R_{En}

Layer 2	
p Waveguide	A_{pm} & B_{pm}
s Waveguide	A_{sm} & B_{sm}
Layer 3	
TM Diffraction	T_{Mn}
TE Diffraction	T_{En}

Amplitudes P and S can be set as desired but all the rest must be found. We follow a usual method for matching infinite sets of plane and waveguide waves [25]. First we set the fields we intend to match equal to each other and multiply through by $e^{-ik_x^{(l)}x}$. Then we integrate both sides over a single period of the structure. This gives

$$\int_0^d e^{ik_x^{(n)}x} e^{-ik_x^{(l)}x} dx = \delta_{nl} d \tag{2.14}$$

on the side of layers 1 or 3. As for layer 2 there are terms of the form:

$$\int_0^d e^{-ik_x^{(l)}x} \begin{cases} C_m e^{i\alpha_1 x} + D_m e^{-i\alpha_1 x} & x < d_1 \\ G_m e^{i\alpha_2 x} + J_m e^{-i\alpha_2 x} & x > d_1 \end{cases} dx \tag{2.15}$$

At this point we reduced the system to a set of eight matrix equations, one for each x and y component of the E and H fields on the upper and lower boundaries. Then using block matrices we reduce those eight equations to these four:

$$\hat{X}^{Ax}\boldsymbol{A} + \hat{X}^{Bx}\boldsymbol{B} + \widehat{K}^{Rx}\boldsymbol{R} = \boldsymbol{D}^x \tag{2.16}$$

$$\hat{X}^{y}(\boldsymbol{A} + \boldsymbol{B}) + \widehat{K}^{Ry}\boldsymbol{R} = \boldsymbol{D}^y \tag{2.17}$$

$$\widehat{W}^{Ax}\boldsymbol{A} + \widehat{W}^{Bx}\boldsymbol{B} + \widehat{K}^{Tx}\boldsymbol{T} = \boldsymbol{0} \tag{2.18}$$

$$\widehat{W}^{Ay}\boldsymbol{A} + \widehat{W}^{By}\boldsymbol{B} + \widehat{K}^{Ty}\boldsymbol{T} = \boldsymbol{0} \tag{2.19}$$

Where the $\hat{X}$s and $\widehat{W}$s contain matrices with entries similar to Eqn. (2.14) while the $\widehat{K}$s are 2x2 block matrices of diagonal matrices containing coefficients due to angles, derivatives, and the like.

These four equations can be reduced further to a single equation:

$$\widehat{M}\boldsymbol{V} = \boldsymbol{D} \tag{2.20}$$

$$\widehat{M} = \begin{pmatrix} \hat{X}^{Ax} & \hat{X}^{Bx} & \widehat{K}^{Rx} & \hat{0} \\ \hat{X}^{y} & \hat{X}^{y} & \widehat{K}^{Ry} & \hat{0} \\ \widehat{W}^{Ax} & \widehat{W}^{Bx} & \hat{0} & \widehat{K}^{Tx} \\ \widehat{W}^{Ay} & \widehat{W}^{By} & \hat{0} & \widehat{K}^{Ty} \end{pmatrix} \tag{2.20a}$$

$$\boldsymbol{V} = \begin{pmatrix} \boldsymbol{A} \\ \boldsymbol{B} \\ \boldsymbol{R} \\ \boldsymbol{T} \end{pmatrix} \ \& \ \boldsymbol{D} = \begin{pmatrix} \boldsymbol{D}^{x} \\ \boldsymbol{D}^{y} \\ \boldsymbol{0} \\ \boldsymbol{0} \end{pmatrix} \tag{2.20c/d}$$

At this point it seems to be a simple task to invert $\widehat{M}$ to solve for $\boldsymbol{V}$, however when using any roots that decay significantly in layer 2, $\widehat{M}$ quickly becomes so poorly conditioned that even double precision isn't enough to produce anything but zeros. The major issue is the matrix $\widehat{H}$ and its inverse contained within the $\widehat{W}$s, where $H_{ml} = e^{ik_z^{(m)}h}\delta_{ml}$ and h is the height of layer 2. This issue can be resolved by using the transfer matrix method we developed.

In this method, we consider each boundary independently to find how an incident wave is converted into outgoing waves. Then we propagate and feed the outgoing waves as incident onto the other boundary and so on, which forms an iterative process.

The full set of waves coming off the upper and lower boundaries can be found by constructing the formulas:

$$\boldsymbol{R} = \boldsymbol{RI} + \hat{R}\hat{P}\boldsymbol{B} \tag{2.21}$$

$$\boldsymbol{A} = \boldsymbol{AI} + \hat{A}\hat{P}\boldsymbol{B} \tag{2.22}$$

$$\boldsymbol{B} = \hat{B}\hat{P}\boldsymbol{A} \tag{2.23}$$

$$\boldsymbol{T} = \hat{T}\hat{P}\boldsymbol{A} \tag{2.24}$$

Here $\boldsymbol{RI}$ ($\boldsymbol{AI}$) is a vector containing the amplitudes of diffraction (waveguide) waves created as a direct result of the incident waves coming from the top medium. $\hat{A}$ and $\hat{B}$ are matrices that convert a waveguide wave amplitude vector into a counter-propagating waveguide wave amplitude vector on the upper and lower boundaries respectively. $\hat{R}$ and $\hat{T}$ convert waveguide wave amplitude vectors into reflected and transmitted wave amplitude vectors respectively. $\hat{H}$ is used to propagate the waveguide vectors down or up the structure.

Substituting $\boldsymbol{B}$ into the formula for $\boldsymbol{A}$ we find:

$$\boldsymbol{A} = \boldsymbol{AI} + \hat{A}\hat{P}\hat{B}\hat{P}\boldsymbol{A} = \boldsymbol{AI} + \widehat{RT}\boldsymbol{A} \tag{2.25}$$

Solving for $\boldsymbol{A}$:

$$\boldsymbol{A} = \left(\hat{1} - \widehat{RT}\right)^{-1}\boldsymbol{AI} \tag{2.26}$$

Then to avoid taking the inverse we expand Eq. (2.26) to finally get to the equation:

$$\boldsymbol{A} = \left(\hat{1} + \widehat{RT} + \widehat{RT}^2 + \widehat{RT}^3 + \cdots\right)\boldsymbol{AI} \tag{2.27}$$

Here $\widehat{RT}$ is a matrix, which we call a *round-trip matrix*. It propagates a set of modes at the top boundary to the bottom of layer 2, reflects them, propagates them back and reflects them once more. The expansion (2.27) can be understood as a sum of a series of roundtrips and eliminates the evanescent modes as they decay. This is the root of the effectiveness of the method.

To use this method we must start by finding $\boldsymbol{RI}$ and $\boldsymbol{AI}$. Consider a two-layer system consisting of layers 1 and 2 only. In this case, we deal with P, S, R, and A coefficients. We again matched the x and y components of the E and H fields on the boundary by multiplying by $e^{-ik_x^{(l)}x}$ and integrating. This time having just the four boundary conditions we only get two equations on the first block matrix system:

$$\hat{\chi}^x\boldsymbol{AI} + \hat{K}^{Rx}\boldsymbol{RI} = \boldsymbol{D}^x \tag{2.28}$$

$$\hat{\chi}^y\boldsymbol{AI} + \hat{K}^{Ry}\boldsymbol{RI} = \boldsymbol{D}^y \tag{2.29}$$

Thus we recreate Eqn. (2.20) as a 2x2 system making the inversion even simpler, and without a $\widehat{W}$ there is no $\widehat{H}$ and thus $\widehat{M}$ is not poorly conditioned.

The next step is to find $\hat{B}$ and $\hat{T}$. Consider the boundary between layers 2 and 3. In this case we have a set of incident waveguide waves, A, reflected waveguide waves, B, and transmitted diffraction waves, T. Using these waves the system only changes slightly to become:

$$\hat{\chi}^x\boldsymbol{B} + \hat{K}^{Tx}\boldsymbol{T} = \hat{D}^{Ax}\boldsymbol{A} \tag{2.30}$$

$$\hat{\chi}^y\boldsymbol{B} + \hat{K}^{Ty}\boldsymbol{T} = \hat{D}^{Ay}\boldsymbol{A} \tag{2.31}$$

The $\boldsymbol{A}$s will be defined later, the $\hat{D}$s are constructed in the same way as the $\hat{\chi}$s, and the $\hat{K}$s are the same sans slight differences due to material choice on the upper and lower boundaries.

Next, we returned to the boundary between layers 1 and 2. This time the incident waves being waveguide waves. The resultant equations are the same as Eqns. (2.30)-(2.31) except $B \rightarrow A$, $A \rightarrow B$, and $T \rightarrow R$.

Now we need to use Eqns. (2.28)-(2.31) to create matrices that directly convert a set of incident waves to reflected and transmitted waves.

$$\widehat{M}^{-1}\boldsymbol{D} = \boldsymbol{V} = \begin{pmatrix} \boldsymbol{AI} \\ \boldsymbol{RI} \end{pmatrix} \tag{2.32}$$

$$\widehat{M}\begin{pmatrix} \boldsymbol{B} \\ \boldsymbol{T} \end{pmatrix} = \begin{pmatrix} \widehat{D}^{Ax} \\ \widehat{D}^{Ay} \end{pmatrix}\boldsymbol{A} \tag{2.33}$$

$$\therefore$$

$$\widehat{M}^{-1}\begin{pmatrix} \widehat{D}^{Ax} \\ \widehat{D}^{Ay} \end{pmatrix} = \begin{pmatrix} \widehat{B} \\ \widehat{T} \end{pmatrix} \tag{2.34}$$

To do this we need the $\widehat{M}^{-1}$ associated with each set of equations, the general form being:

$$\widehat{M}^{-1} = \begin{pmatrix} \left(\hat{\chi}^x - \widehat{K}^x \widehat{K}^{y^{-1}} \hat{\chi}^y\right)^{-1} & -\hat{\chi}^{x^{-1}} \widehat{K}^x \left(\widehat{K}^y - \hat{\chi}^y \hat{\chi}^{x^{-1}} \widehat{K}^x\right)^{-1} \\ -\widehat{K}^{y^{-1}} \chi^y \left(\hat{\chi}^x - \widehat{K}^x \widehat{K}^{y^{-1}} \hat{\chi}^y\right)^{-1} & \left(\widehat{K}^y - \hat{\chi}^y \hat{\chi}^{x^{-1}} \widehat{K}^x\right)^{-1} \end{pmatrix} \tag{2.35}$$

Doing Eqns. (2.33) and (2.34) again for the other side, mutatis mutandis, yields the $\hat{A}$ and $\widehat{R}$ conversion matrices.

Results and Conclusions

For convergence one seems to needs to truncate the infinite system of equations at about $|k_z|^2 \approx \left(1\ \text{Å}\right)^{-2}$ which occurs at various N_{tr} waveguide modes. This means that taking just one propagating waveguide mode [23] is not enough for determining the exact optical properties of these structures. The evanescent modes may not contribute to the determination of the spectral positions of the resonances in subwavelength structures, but they determine the power distribution at interfaces between layers. Additionally the possibility of including multiple modes in our method allows for consideration of large period structures and the establishing of the exact conditions under which the metamaterial approximations fail.

Currently, there is a strong interest in applicability of effective medium approximation for describing fields in metamaterials. To evaluate the correctness of the results of this approximation, one has to compare it to an exact calculation. In Chapter 3 we demonstrate that the effective medium approximation and our new method lead to close results for subwavelength structures.

To conclude, we have developed a new transfer matrix method for calculating the fields in metal-dielectric parallel-plate arrays. This method allows reaching convergence and obtaining reliable results. We apply this method to model metasurface wave plates introduced in Chapter 3.

Chapter 3

Light Polarization Control with Square Nanowire Metasurfaces

Polarization manipulation constitutes a large portion of what optical components do. The large majority of wave plates operate on one simple principle, in one polarization the light moves more slowly than in the orthogonal polarization. This phenomenon, known as birefringence, is well understood, however the two speeds of light are never that far from each other in natural materials leading to a requirement that the component be somewhat thick to accommodate the large number of wavelengths needed to produce a full 180° flip in relative phase [26]. The modern push into metasurface photonics has produced a myriad of amazing ideas into optics [27-29]. This includes some polarization converters, some of which include metasurface cavities that can reduce the required thickness to a mere fraction of a micron [22, 30-33]. And some single surface structures have been proposed that can shrink that even further [34-37]. All of which so far require complex structures that are tricky to fabricate. Recently it has been shown experimentally that a simple gold nanowire based metamaterial produced polarization rotation with only 350 nm [38].

Here we are looking at a thin layer of the parallel plate structure described above were the period is taken to be far sub wavelength. At this extreme this material could either be considered, as stated, a thin layer of a parallel plate metamaterial, or a monolayer of a nanowire array. Nanowire arrays such as this are well known as being the simplest polarizers. However, in this case the structure is made to act as a wave plate in near IR and visible range. This is achieved by using both the epsilon near pole (ENP) and epsilon near zero (ENZ) transitions that occur in orthogonal directions as the volumetric metal fraction changes from 0 to 1. These transitions occur because the metal's permittivity is negative, its absorption is low, and a high index dielectric is between wires. When thicker, this material supports a large number of Fabry-Perot (FP) resonances allowing potentially for multiple polarization rotation points.

Structure

Consider a parallel-plate metal-dielectric array with period $d = d_m + d_d$, where $d_m = fd$ and $d_d = (1 - f)d$ are the thicknesses of the metal and dielectric layers (Fig. 3.1 (a)). The dielectric permittivities are ε_m and $\varepsilon_d = n_d^2$ for the metal and dielectric and f is the volumetric metal fraction. As stated in Chapter 2, the dispersion of the photonic states is described by the Kronig-Penney equation, and at normal incidence by Eqs. 2.12 and 2.13.

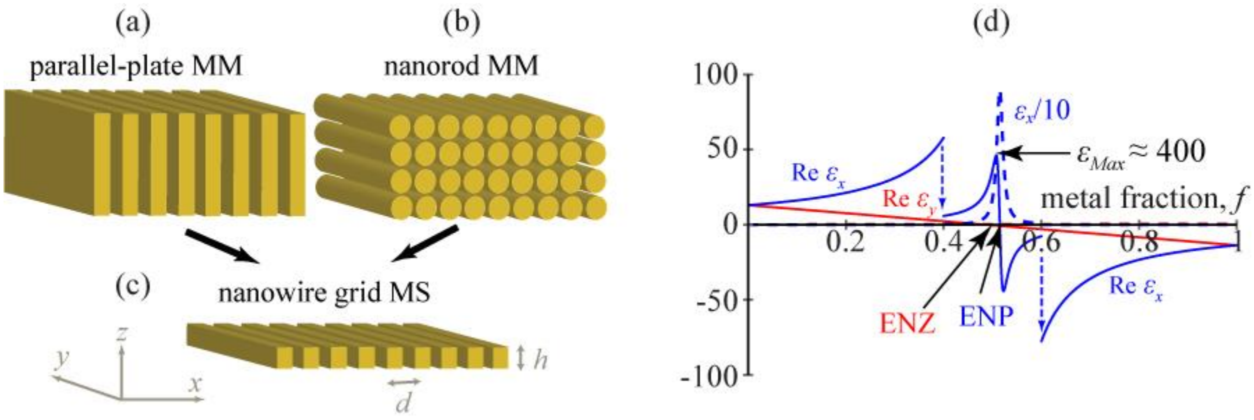

Fig. 3.1: Schematic of the structure and its typical dielectric response. (a), (b), (c) Correspondence between the parallel-plate and the nanorod metamaterials and the monolayer nanowire grid metasurface considered in this chapter. (d) Dielectric permittivities ε_x (blue for real and dashed blue for imaginary parts) and ε_y (red) as functions of metal fraction at $\hbar\omega = 2.2\, eV$ for silver/GaAs metasurface, featuring ENP and ENZ.

The dispersion Eqs. (2.12-13) have an infinite number of solutions. In a subwavelength array $k_0 d \ll 1$, only modes with $\alpha_{m,d} d_{m,d} \ll 1$ efficiently couple to external waves. In this case, the tangent functions in Eqs. (2.12-13) can be substituted by their arguments. Only Eq. (2.12) leads to reasonable dispersion equations in this limit, which are given by $k_z^2 = k_0^2 \varepsilon_x$ for TM fields (electric field along x-axis in Fig. 3.1 (a), (c)) and $k_z^2 = k_0^2 \varepsilon_y$ for TE fields (electric field along y-axis). The effective dielectric permittivities are given by

$$\varepsilon_x^{-1} = \varepsilon_m^{-1} f + \varepsilon_d^{-1}(1-f), \varepsilon_y = \varepsilon_m f + \varepsilon_d (1-f). \tag{3.1}$$

Hence in the subwavelength case the array forms a metamaterial, with 3 bright modes, whose fields closely follow the effective medium approximation and all the other photonic states are dark plasmonic modes. Below we use Eqs. (3.1) for effective medium calculations and model given in Fig. 3.1 (a) and (c) for exact calculations, but the same ideas apply to the nanorod metamaterials or metasurfaces. Note that the structures we consider here are different in principle from the structures considered in [38, 39], where the optic axes were perpendicular to the plane of the metasurfaces and the dielectric response in the plane of the metasurface was isotropic, which required large angles of incidence to achieve polarization manipulation. In this chapter, we consider structures with optic axes in the plane of the metasurfaces perpendicular to the incidence direction, and anisotropy of the dielectric properties *in the plane* of the metasurface is crucial for the effects we predict.

Metamaterial Approximation

This data is decently represented by using a metamaterial approximation in which the epsilons in eqs. (3.1) are taken and the structure is assumed to be homogeneous. Note that at normal incidence the dielectric properties along the z axis ($\varepsilon_z = \varepsilon_y$ for parallel plates and

$\varepsilon_z = \varepsilon_x$ for nanorods) do not affect the response of the metasurface, which removes the principal difference between the nanorods and parallel-plates.

Going from pure dielectric to pure metal, waves who's polarization lies against the optical axis, in the y direction, called ordinary waves, will see the material as a simple linear combination of the two materials dielectric constants leading to an ENZ transition. However, for waves polarized with the optical axis, in the x direction, called extraordinary waves, the material's response can be characterized as the inverse of the sum of inverses leading to an ENP transition. For ordinary waves, the permittivity trends down as metal fraction increases and for extraordinary waves the permittivity trends up, except in a small region around the ENP transition where absorption takes over. These trends lead to the increase and decrease of effective wavelength $\lambda_0/\sqrt{\varepsilon_i}$ respectively. Note that the values of ε_x can get very high, for example, Re $\varepsilon_x \approx 400$ in Fig. 3.1(d). This is an artifact of the effective medium approximation, since for such values of $k_z/k_0 = \sqrt{\varepsilon_{Max}}$ the condition $\alpha_{m,d} d_{m,d} \ll 1$ is not satisfied.

The energies of the FP resonances depend strongly on f, such that the nth extraordinary FP (e-FP$_n$) mode may intersect mth ordinary FP (o-FP$_m$) resonance if $n > m$ at energies which we denote as $E_{hw,mn}$, where "hw" stands for "half-wave plate" as will be explained below.

In Fig. 3.2(a) we plot reflectivity for a very thin metasurface with $h = 30$ nm. Only one extraordinary e-FP$_1$ resonance with is visible. Higher order resonances are positioned closer to ENP and are extremely faint due to strong absorption in the effective medium at ENP. The only ordinary wave resonance present has $n = 0$ at the ENZ transition. The e-FP$_1$ and the ENZ intersect at $\hbar\omega = E_{hw,01}$ as indicated by the black dot. We show reflectivity for thicker metasurfaces $h = 100$ nm and 150 nm in Fig. 3.2 (b)-(c). As one can see the e-FP$_1$ shifts to lower energies and higher order extraordinary resonances become strong. Additionally ordinary resonances appear and intersect with higher order extraordinary resonances at $\hbar\omega = E_{hw,mn}$.

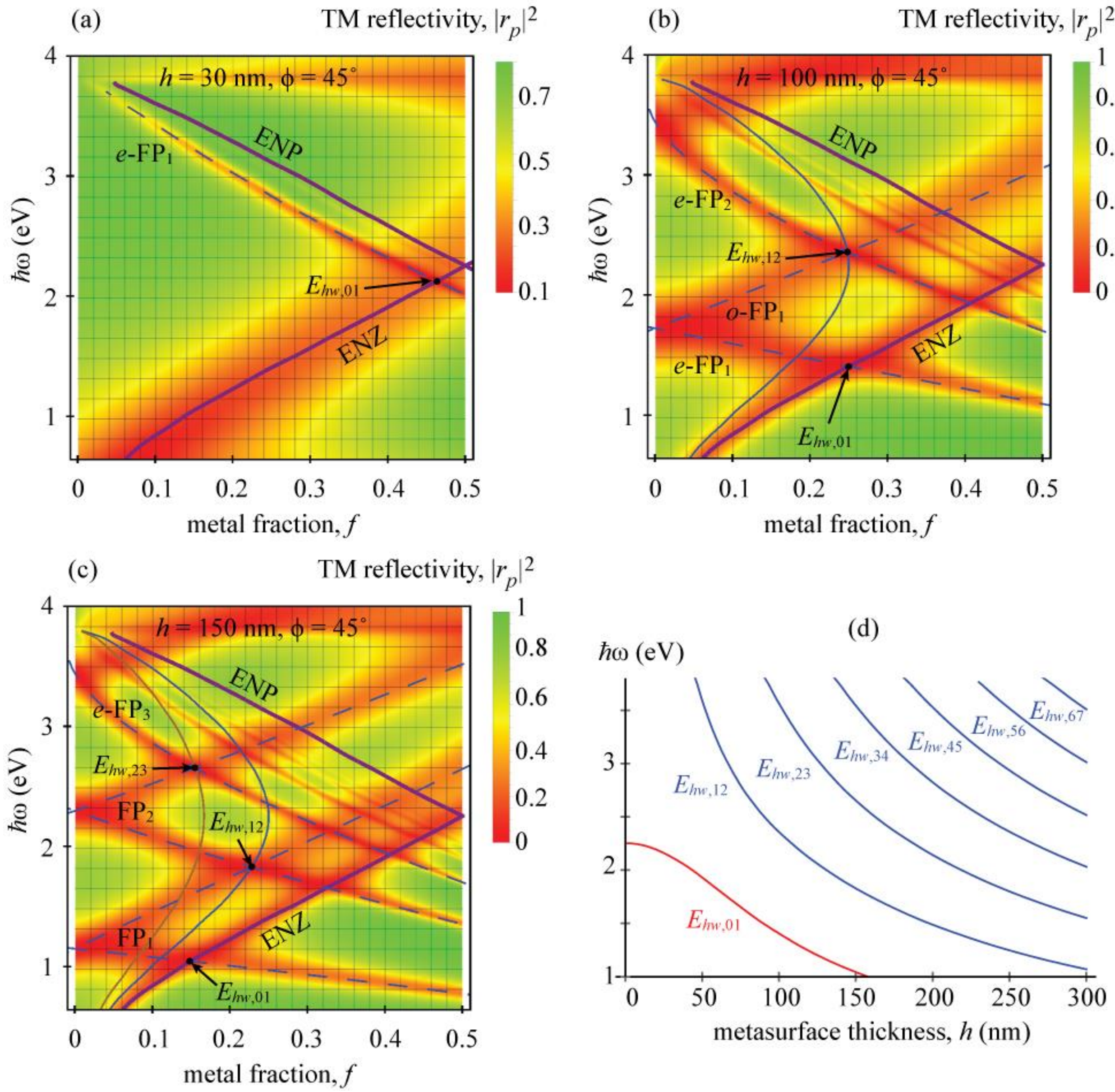

Fig. 3.2: Reflectivity of metasurfaces at $\phi = 45°$. (a) $h = 30\,nm$; (b) $h = 100\,nm$; (c) $h = 150\,nm$. (d) Dependence of the energies $E_{hw,nn+1}$ at which the metasurface is a half-wave plate on metasurface thickness.

We are mainly interested in intersections between the consecutive FP resonances at $E_{hw,nn+1}$. For very thin metasurfaces the intersection between e-FP$_1$ and the ENZ occurs at $f_{01} \approx 0.5$ and with increase of the thickness h shifts down in energy along the ENZ line as shown in Figs. 3.2 (a)-(c). The intersections $E_{hw,nn+1}$ are marked by black dots and as h is increased their energies are reduced. This dependence of $E_{hw,nn+1}$ on metasurface thickness h is shown in Fig. 3.2(d). For thicker metasurfaces more FP resonances and their intersections appear in the plasmonic frequency range of silver (∼1-4 eV).

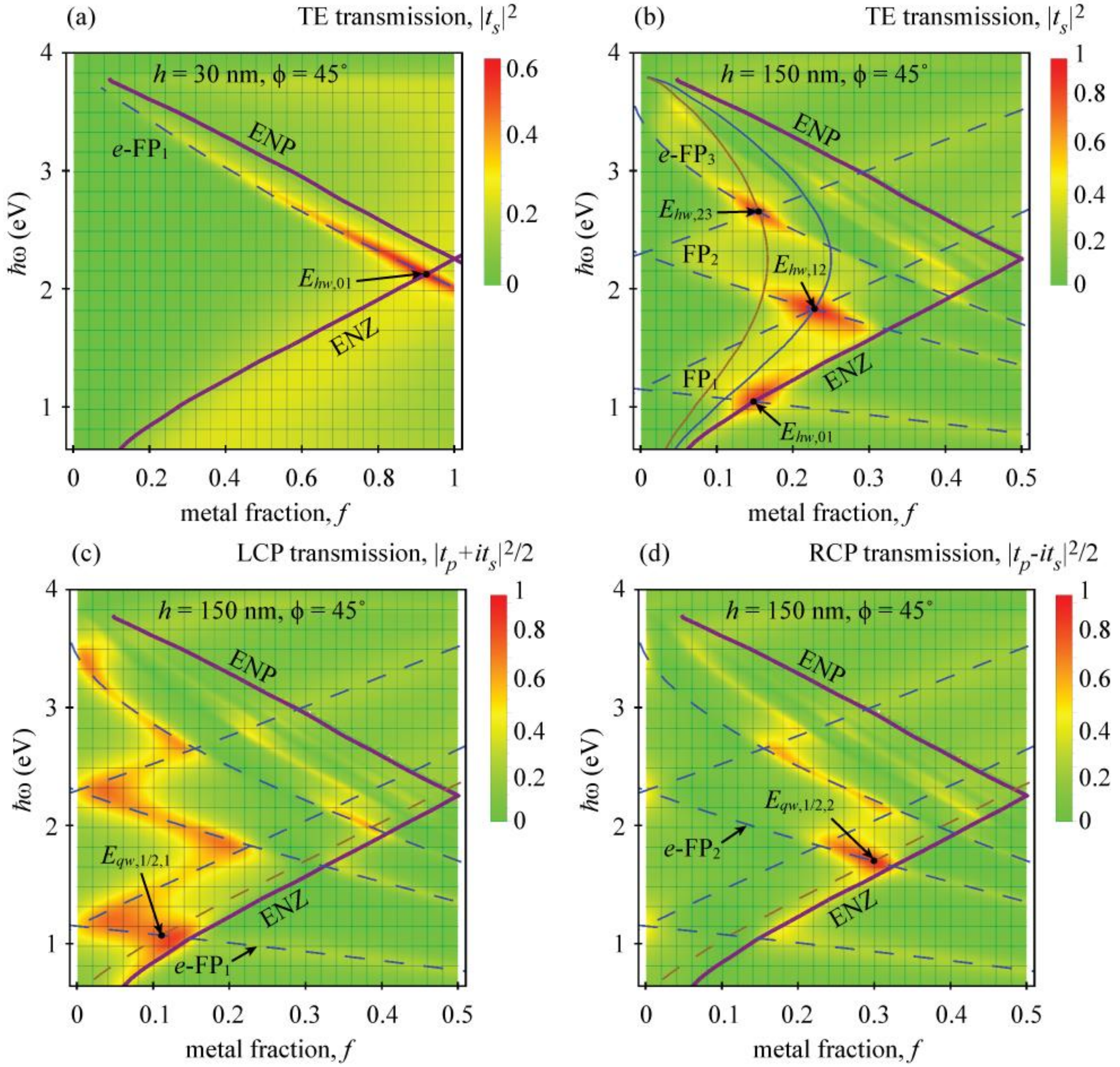

Fig. 3.3 (a), (b) TE transmission for $h = 30\,nm$ and $h = 150\,nm$ in response to TM polarized light. (c), (d) Transmission of left and right circular polarized light in response to TM polarized incidence for metasurface thickness $h = 150\,nm$.

The nature of polarization rotation in the ENZ-ENP structure (Figs. 3.2(a) and 3.3(a)) which we propose here is easy to understand. The electric field of the ENZ ordinary wave directed along the y-axis (see schematics in Fig. 3.1 (a)-(c)) exhibits no phase change, while the extraordinary fields directed along the x-axis oscillate with wavelength $\lambda_x = \lambda_0/\sqrt{\varepsilon_{Max}} = 2h$, providing the required phase difference for the wave-plate effect in an extremely thin metasurface. We call this structure an *ultrathin ENZ-ENP wave plate*.

A larger thickness $h = 150\,\text{nm}$ metasurface (Fig. 3.3 (b)) has intersections at $\hbar\omega = E_{hw,nn+1}$ that lead to peaks with transmission $T > 0.95$ in TE. Further investigating this structure, we can find conditions in which it exhibits quarter-wave-plate behavior, converting linearly polarized incident radiation to circularly polarized transmission. For $h = 150$ nm the efficient close-to-90% conversion into left-circular polarized (LCP) radiation happens at $E_{qw,1/2,1}$, while 90% conversion into right-circular polarized (RCP) occurs at $E_{qw,1/2,2}$. This high-efficiency conversion from linear to circular polarization indicates that the metasurfaces proposed here can acquire torques from the incident radiation with power $P_{inc} =$ mW of about $\tau \approx P_{inc}/\omega$ in the 10^3 pN $\cdot$ nm range, similar to the optical torque wrench structures previously proposed [40]. At the same time these metasurfaces have moments of inertia of comparable magnitudes, despite being composed of heavy Au atoms due to reduced dimensionality. This introduces the possibility of high-rpm rotation of plasmonic metal nanostructures.

Semi-analytical Solution

We use our recently developed numerical method, which I describe in the previous Chapter, to solve Maxwell's equations semi-analytically for the nanostructure shown in Figs. 3.1 (a) and (c). To do so we first find the solution to the Kronig-Penney equation, which for normal incidence is given by Eqs. (2.12-13). The effective permittivity may become large at ENP, which leads to $k_z \approx \alpha_{m,d} \gg 1/d_m$, violating the applicability conditions for the effective medium approximation. We compare the exact solution of Eq. (2.12-13) for the bright extraordinary modes in the structure with period $d = 50$ nm with the effective medium dispersion, obtained using ε_x from Eq. (3.1) (see Fig. 3.1(d)). We are especially interested in deviations of the mode propagation wave vector k_z, since $k_z = n\pi/h$ is the condition for the extraordinary FP resonances.

We provide the three most extreme examples of such deviations for the two resonances: the e-FP$_1$ mode at $h = 30$ nm which requires $k_z = \pi/(30\text{ nm})$ (shown as the right red dashed line in panels of Fig. 3.4) and the e-FP$_3$ mode at $h = 150$ nm requiring $k_z = 3\pi/(150\text{ nm})$ (the left red dashed line in Fig. 3.4). The blue curves in Fig. 3.4 represent the exact solution of Eq. (2.12-13), while the green curves are the effective medium approximation. In Fig. 3.4(a) for $f = 0.3$ the exact solution intersects the $n\pi/h$ lines at lower frequencies than the effective medium approximation, as indicated by the blue and green arrows. The real part of the exact solution does not intersect the $k_z = \pi/(30\text{ nm})$ line, but comes close to it at $\hbar\omega = 2.33$ eV, so the resonance at this frequency should be expected.

In Fig. 3.5(b) for $f = 0.4$ we see that the exact dispersion coincides with the effective medium dispersion at $k_z = 3\pi/(150\text{ nm})$. Meanwhile, for the exact dispersion at $\operatorname{Re} k_z = \pi/(30\text{ nm})$ two resonances exist within close proximity at $\hbar\omega = 2.1$ eV and $\hbar\omega = 2.2$ eV due to back-bending, instead of a single frequency for the effective medium at $\hbar\omega = 2.33$ eV. As can be seen from Fig. 3.4(c) the high-frequency root from the back-bending pair with $\operatorname{Re} k_z = \pi/(30\text{ nm})$ has much higher damping as it is overwhelmed by large $\operatorname{Im} k_z$ (represented by the dashed blue line), leaving only the low-frequency root as a resonance. It is important to note that this is always the case for the effective medium approximation regardless of f. For $f = 0.5$ the exact solution intersects the $n\pi/h$ lines at higher frequencies than the effective medium dispersion.

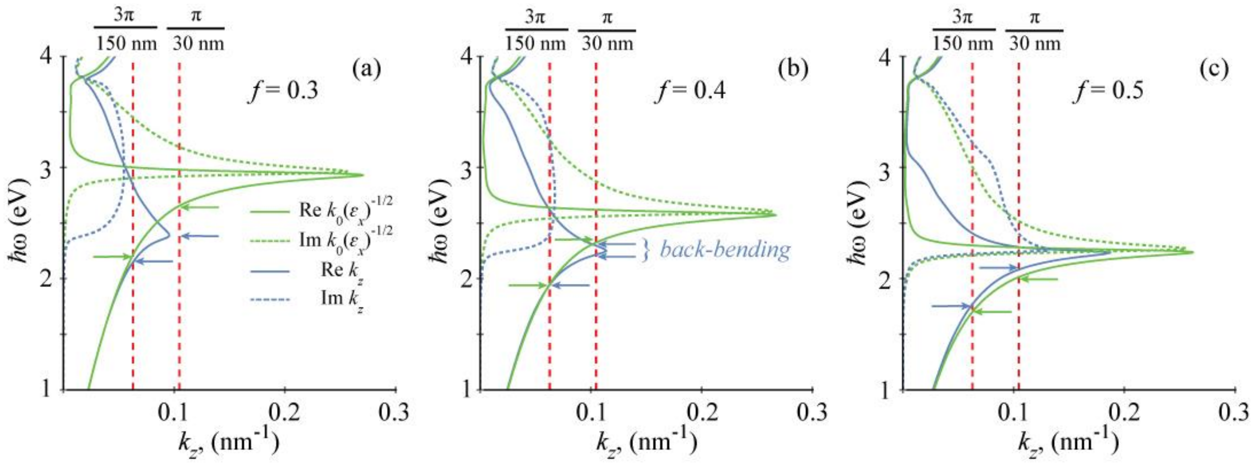

Fig. 3.4 Comparison of the exact solution $\omega(k_z)$ of Eq. (1) for period $d = 50\, nm$ and the effective medium approximation (the inverse function of $k_0\sqrt{\varepsilon_x(\omega)}$) with (a) $f = 0.3$; (b) $f = 0.4$; (c) $f = 0.5$.

This analysis directly translates into the optical response of the metasurface in the full solution of Maxwell's equations according to semi-classical method of Ref. [38] illustrated in Fig. 3.5. Panels (a) and (b) show the reflectivity of the structure at $h = 30$ nm and $h = 150$ nm respectively, which correspond directly to the effective medium calculations shown in Fig 3.2 (a) and (c). Similarly, panels (c) and (d) in Fig. 3.5 show TE transmittance in direct comparison to Fig. 3.4(a) and (b). The ramifications of the disparity between k_z calculated exactly and in the effective medium approximation near the ENP as outlined in Fig. 3.4 make themselves apparent in Fig.3.5 by the higher degree of curvature and back-bending in the energy as a function of metal fraction f for the e-FP$_1$ at $h = 30\, nm$ and e-FP$_3$ at $h = 150\, nm$ (Fig. 3.5 (a) and (b) respectively). This results in minor shifts in the parameters and insignificant changes in the magnitude for the half-wave (Fig. 3.5 (c) and (d)) and quarter-wave plate behavior (not shown) as manifested by the TE transmission at $\hbar\omega = E_{hw,nn+1}$.

Note that for calculations in this chapter we use the dielectric permittivity of silver [41] and a dielectric with refractive index $n_d = \sqrt{\varepsilon_d} = 3.6$, which corresponds to GaAs.

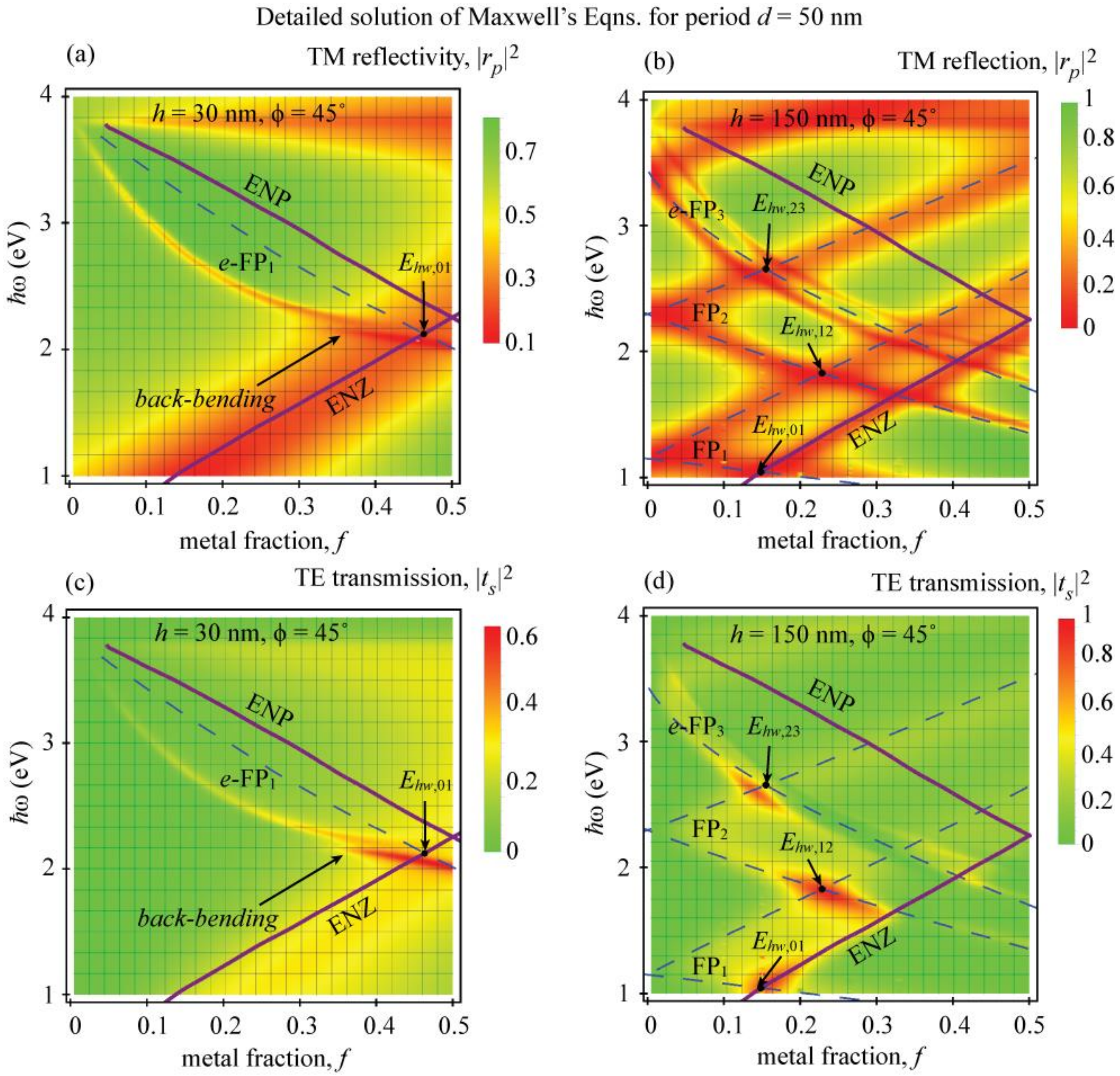

Fig. 3.5 Optical properties on the metasurface shown in (Fig. 3.1(c)) according to the semi-analytical solution of Maxwell's equations. (a), (b) Reflectivity of the metasurface at $\phi = 45°$ for $h = 30\,nm$ and $h = 150\,nm$; (c), (d) TE transmission of the same metasurfaces.

Conclusion

In this Chapter I used the method described in Chapter 2 to theoretically and numerically predict the optical response of a nanowire grid array. Using the full solutions of Maxwell's equations, beyond a metamaterial approximation, show that it acts as an ultrathin nanoscopic wave plate. The correctness of the method and calculations is confirmed by the similarity between the results of the full calculations and metamaterial approximation within region of applicability for the metamaterial approximation.

Chapter 4

Chandezon's Method

The following relies very heavily on the works of Chandazon et. al. [15] and S. J. Elston et. al. [42] but was fully implemented in a program as part of my work, thus I am reproducing its derivation here.

As stated in the introduction, Chandazon's method is a method of transforming the space around a structure such that the structure is flat, solving Maxwell's wave equations in the curved space, and matching the resulting waves at the now flat boundary. We use this method to study structures with arbitrary profiles. First we define the structure with a periodic function $y = a(x)$ with period d in Euclidean coordinates (Fig. 4.1). With an incident wave vector $\boldsymbol{k}$ at an angle θ off the y axis and angle ϕ between the x-y-plane and incident plane.

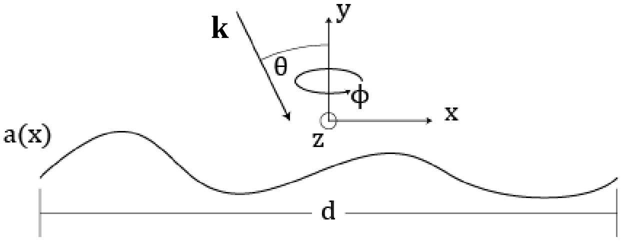

Fig. 4.1: Structure and Euclidian Basis, showing the incident wave vector **k**, its angle off the normal, θ, angle off the x-y-plane, ϕ, the basis vectors x, y, and z, the boundary function $y = a(x)$, and its period d.

Here we can define two polarizations, transverse electric (TE) and transverse magnetic (TM) where the respective fields only have components perpendicular to the plane of incidence. In either case, we take the complex time independent incident field to be:

$$|\boldsymbol{F}| = \exp\Big(i\big(k_x x - k_y y + k_z z\big)\Big), \tag{4.1}$$

where k_x, k_y, and k_z are absolute value of the components of $\boldsymbol{k}$ and $\boldsymbol{F}$ represents either the electric (TE) or magnetic (TM) field. The scattered far field should also be defined in a standard form

$$\textstyle\sum_n R_n \exp\big(i(\alpha_n x + \beta_n y + k_z z)\big), \tag{4.2}$$

in reflection where $\alpha_n = k_x + \frac{2\pi n}{d}$, $\beta_n = \sqrt{\boldsymbol{k}^2\epsilon_s - \alpha_n^2 - k_z^2}$, and ϵ_s is the permittivity of the media the wave is propagating; and

$$\textstyle\sum_n T_n \exp\big(i(\alpha_n x - \beta_n y + k_z z)\big), \tag{4.3}$$

in transmission where the sum is over all far field diffraction orders.

Having defined the structure and far field, we now move to construct a coordinate system in which the surface is flat. For scalars, this is simple:

$$u = x, v = y - a(x), w = z. \tag{4.4}$$

However, defining vectors is a bit more complicated, in order to reproduce curl, required for Maxwell's equations, while maintaining simple formulae two sets of vectors are needed, the contravariant

$$\boldsymbol{\eta}^1 = \hat{\boldsymbol{\imath}}, \qquad \boldsymbol{\eta}^2 = \hat{\boldsymbol{\jmath}} - a'\hat{\boldsymbol{\imath}}, \qquad \boldsymbol{\eta}^3 = \hat{\boldsymbol{k}}, \tag{4.5}$$

and the covariant

$$\boldsymbol{\eta}_1 = \hat{\boldsymbol{\imath}} + a'\hat{\boldsymbol{\jmath}}, \qquad \boldsymbol{\eta}_2 = \hat{\boldsymbol{\jmath}}, \qquad \boldsymbol{\eta}_3 = \hat{\boldsymbol{k}}, \tag{4.6}$$

where $\hat{\imath}$, $\hat{\jmath}$, and $\hat{k}$ are unit vectors in the x, y, and z directions respectively. These vectors then allow cross products, and thus Maxwell's equations to be modified as follows

$$\boldsymbol{\nabla} \times \boldsymbol{F} = \left(\boldsymbol{\eta}^1 \frac{\partial}{\partial u} + \boldsymbol{\eta}^2 \frac{\partial}{\partial v} + \boldsymbol{\eta}^3 \frac{\partial}{\partial w}\right) \times \left(F_u \boldsymbol{\eta}_1 + F_v \boldsymbol{\eta}_2 + F_w \boldsymbol{\eta}_3\right), \tag{4.7}$$

while the time derivative is unaffected, simply producing a $-ik$ term due to its complex exponential nature. Due to that same nature, as well as the translational symmetry in the w/z direction

$$\frac{\partial}{\partial w} = ik_z. \tag{4.8}$$

From here we use the fact that we only need two boundary conditions for each of two polarizations at any given boundary to reduce the problem further, and because both E and H fields parallel to a surface are continuous across the boundary, we will use the fields

$$\begin{gathered} H_{||} = (1 + (a')^2)H_u + a'H_v, \quad E_w = E_z, \\ E_{||} = (1 + (a')^2)E_u + a'E_v, \quad \text{and} \quad H_w = H_z. \end{gathered} \tag{4.9}$$

This means that, with a bit of manipulation, Maxwell's wave equations can be written in the form

$$\widehat{U}\boldsymbol{F} = \frac{\partial}{\partial v}\boldsymbol{F}, \tag{4.10}$$

Where

$$\widehat{U} = \begin{pmatrix} \frac{\partial}{\partial u}\frac{a'}{1+(a')^2} & 0 & \frac{\partial}{\partial u}\frac{k_z}{k(1+(a')^2)} & ik\epsilon + \frac{\partial}{\partial u}\frac{i}{k(1+(a')^2)}\frac{\partial}{\partial u} \\ 0 & \frac{a'}{1+(a')^2}\frac{\partial}{\partial u} & \frac{-i\left(k^2\epsilon - k_z^2\right)}{k(1+(a')^2)} & -\frac{k_z}{k(1+(a')^2)}\frac{\partial}{\partial u} \\ -\frac{\partial}{\partial u}\frac{k_z}{k\epsilon(1+(a')^2)} & -ik - \frac{\partial}{\partial u}\frac{i}{k\epsilon(1+(a')^2)}\frac{\partial}{\partial u} & \frac{\partial}{\partial u}\frac{a'}{1+(a')^2} & 0 \\ \frac{i\left(k^2\epsilon - k_z^2\right)}{k\epsilon(1+(a')^2)} & \frac{k_z}{k\epsilon(1+(a')^2)}\frac{\partial}{\partial u} & 0 & \frac{a'}{1+(a')^2}\frac{\partial}{\partial u} \end{pmatrix}, \quad \boldsymbol{F} = \begin{pmatrix} H_{||} \\ H_w \\ E_{||} \\ E_w \end{pmatrix}. \tag{4.11}$$

Now E_w and H_w need to be defined for the far field waves. The transmitted waves will be of the form

$$F_w = \sum_n T_n \exp\left(i\left(k_z w - \beta_n\left(v - a(u)\right) + \alpha u\right)\right), \tag{4.12}$$

which we can Fourier expand to give

$$F_w = \sum_n T_n \sum_m L_{m-n}(\beta_n) \exp\left(i(\alpha_m u - \beta_n v + k_z w)\right), \tag{4.13}$$

where

$$L_m(f) = \frac{1}{d}\int_0^d \exp\left(-i\left(a(u)f + \frac{2\pi m}{d}u\right)\right). \tag{4.14}$$

The reflected fields look the same *mutatis mutandis*, and for the incident field, $n = 0$ and the amplitude coefficient is assumed to be 1.

The final piece to the puzzle is to note that the matrix that represents Maxwell's equations has only two functions that are dependent on the structure,

$$C(u) = \frac{1}{1+(a')^2}, \text{ and } D(u) = \frac{a'}{1+(a')^2}, \tag{4.15}$$

which can both be Fourier expanded. The same can be done to any solutions to the whole system of equations due to the structure's periodicity. Expanding these two independent sums will allow us to evaluate the derivatives in $\boldsymbol{U}$ and subsequently turn $\widehat{U}$ into a block matrix with each entry an $\infty \times \infty$ matrix. Of course, to solve it we truncate the sums at $\pm N$ creating an $(8N+4) \times (8N+4)$ matrix for which we find the eigenvalues and eigenvectors, r_q and $\boldsymbol{V}_q$. These then allow us to construct the fields present in the medium

$$\boldsymbol{F}(v) = \widehat{M}\widehat{\Phi}(v)\boldsymbol{A}, \tag{4.16}$$

where $\boldsymbol{F}$ is the expanded form of the block vector in eq. 4.12, $\widehat{M}$ is a matrix whose columns are $\boldsymbol{V}_q$, $\widehat{\Phi}$ is a matrix with entries $\Phi_{pq}(v) = \exp\left(ir_q v\right)\delta_{pq}$, and $\boldsymbol{A}$ is an amplitude vector we still need to find via boundary conditions. Now, it is important to point out that in the topmost and bottommost media we will only need those eigenvalues that have positive, or negative imaginary components respectively because these will be the ones that go to zero at infinity. The opposites will approach complex infinity at infinity, and the remaining, those with only real parts have already been defined by 4.14. We should also note that the waves defined in 4.14 are already in the basis of the expanded $\boldsymbol{F}$ vector, meaning that these outward propagating waves can replace the waves that best resemble plane waves. Now, we simply split the $\boldsymbol{F}$ in, my choice being between w and $||$ components. From this we construct boundary condition equations just as was done in chapter two, albeit with significantly fewer diagonal matrices.

As a test of this method I devised a formula to approximate a square wave like structure where $a'(x)$ is a difference of offset Jacobi theta 3 functions to compare it to the photonic crystal method described in Chapter 2. The results look similar (fig. 4.2), but Chandezon's method presents its own computational issues.

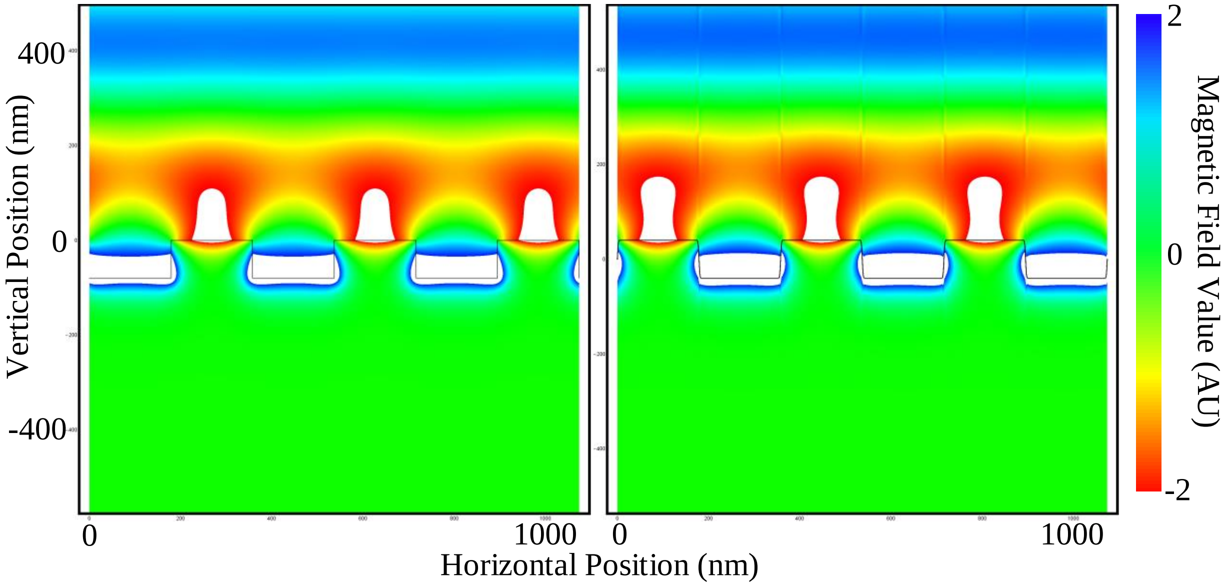

Fig. 4.2: The magnetic field due to normal incident light on an air-gold structure with (a) $d = 358$ nm, $f = 0.5$, and $h = 80$ nm, and (b) a similar structure using C-method with approximately 10 nm transitions between top and bottom flat sections.

As the structure gets closer to the true shape for the photonic crystal, the number of waves required to produce sensible results increased rapidly. However, it is far less prone to conditioning issues, involves finding no solutions to transcendental equations, and allows for much more flexibility in structure types.

Chapter 5

Sine Wave Grating: Optoelectronic Characterization

Plasmon drag effect (PLDE) is an enhancement of photoinduced electric currents in metal films and nanostructures [43-51], associated with excitation of surface plasmon polaritons(SPPs). PLDE presents interest for various applications as it provides an opportunity for direct electrical monitoring of plasmonic elements in electronic and optoelectronic devices and sensors. From a fundamental point of view, the effect can be considered in terms of plasmon-assisted momentum transfer in light–matter interaction in metal [44]. In the first PLDE experiments [50, 51], strong enhancement of photoinduced currents was observed in flat gold and silver films under conditions of surface plasmon polariton resonance in Kretschmann geometry [52]. Significant photo-induced electric effects were reported in rough and nanostructured surfaces under direct illumination, with polarity and magnitude of electric signals dependent on angle of incidence, wavelength of illumination, light polarization, and nanoscale surface geometry [43, 47-49].

The theoretical description of PLDE is based on electromagnetic momentum loss. In a metal nanostructure, the rate of momentum transfer from field to electrons can be found as [44]

$$\bar{f_{L}}_{i} = \frac{1}{2}\sum_{\alpha=\mathrm{x,y,z}} \mathrm{Re}\{P_{\alpha}\partial_{i}E_{\alpha}^{*}\}, \tag{5.1}$$

where $\boldsymbol{P} = \chi\boldsymbol{E}$ is the polarization vector, E is the electric component of the optical field, and χ is the susceptibility of the material. It was recently shown [53] that this approach, modified to take into account the electron thermalization time [54, 55], τ_{therm}, adequately describes the electric currents induced under SPP resonance conditions in flat films. The theory was extended to surfaces with modulated profiles and multi-mode plasmonic excitations [53]. Assuming a relatively small amplitude of surface modulation height, and laminar electric current, the electromotive force (emf) per unit length induced in a plasmonic structure can be presented as a sum of contributions from each mode, with the contribution proportional to the absorbed power Q_m and k-vector of each mode, k_m, as

$$U = \sum_m U_m = \frac{\tau_{therm}}{\tau}\frac{1}{n_e e}\sum_m \frac{\hbar k_m}{\hbar\omega} Q_m, \tag{5.2}$$

where τ is the Drude collision time, and n_e is the electron density.

According to [53], strict numerical calculations (eq. (5.1)) correctly predict the angular position, magnitude and polarity of the photoinduced currents experimentally observed in flat silver films [50] and a gold film with a sine-wave profile [53] at the SPP resonance conditions. However, in both cases, the exact shape of the peak as well as off-resonance signals are not properly described by the theory; and this is tentatively attributed to the effect of roughness in experimental samples. Below, we provide details of our calculations for the sine-wave films, explore limitations of our theoretical approach [53] and the validity of a simplified consideration (equation (5.2)).

The structure under consideration is a 60 nm thick gold film with a sine-wave profile, a period of $d = 538$ nm and a modulation depth 2 h, which we varied, see fig. 5.1(a). The electromagnetic fields in a sine-wave structure are calculated Chandezon's method described above. As expected, simulations predict surface plasmon resonance (SPR) [55] at the incidence angle, θ

$$k_{spp} = \frac{2\pi n}{d} + k_x, \tag{5.3}$$

where $k_x = k\sin(\theta)$ is the x component of the k-vector and n is an integer. The SPP k vector closely corresponds to the estimations for flat films [56],

$$\frac{k_{SPP}}{k} = \xi = \sqrt{\frac{\varepsilon_m \varepsilon_d}{\varepsilon_m + \varepsilon_d}}, \tag{5.4}$$

where ε_m and ε_d are dielectric permittivities for metal and air respectively.

Reflectivity of the film, $R(h,\ \theta,\ \omega)$ was calculated for the whole optical range for various amplitudes of surface modulation, h = 0-50 nm, as a function of incidence angle, θ, and light frequency (Fig. 5.1(b)). Two SP branches are seen, which can be fitted with Eq. (5.3) for $n = -1$ or $+1$, corresponding to the plasmon propagating backward, against k_x, for the low frequency branch and forward, with k_x, for the high frequency branch. These modes join each other at $\theta = 0$ and frequency ~ 2.15 eV, forming a standing plasmon wave with $k_{spp} = \frac{2\pi d^{-1}}{\xi}$.

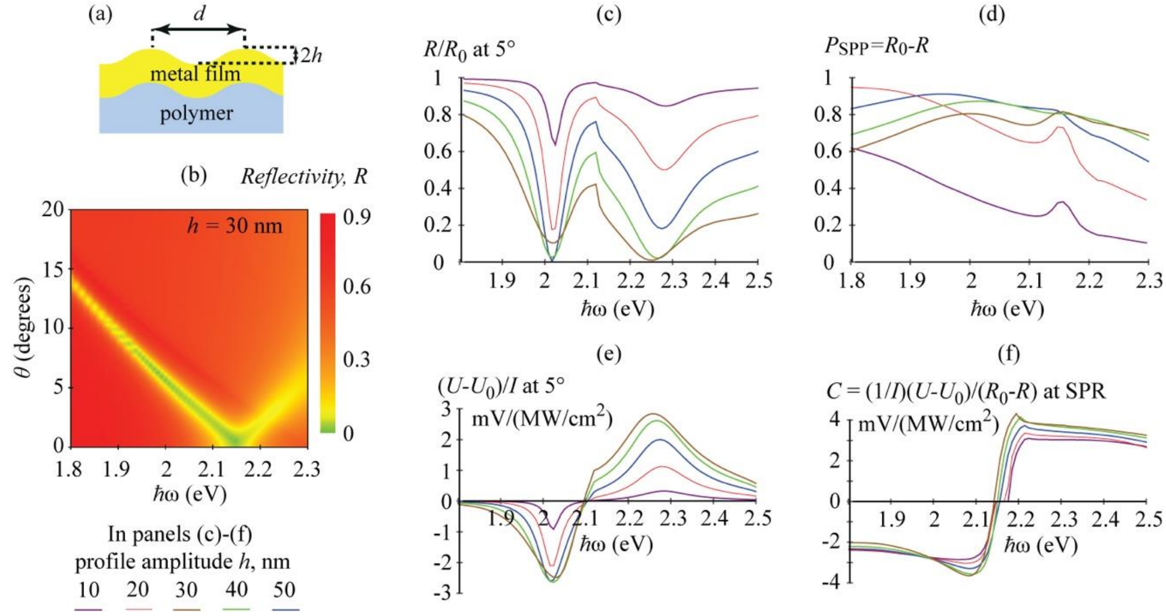

Fig. 5.1: (a) Schematic of the structure; (b) Reflectivity as a function of θ and $\hbar\omega$ for $h = 30$ nm; (c) Normalized reflectivity for $\theta = 5°$ for different modulation amplitudes h as color coded in the bottom left corner of the figure; (d) Frequency spectrum of SPP losses for different h; (e) PLDE emf spectrum corresponding to reflectivity in panel (c); (f) Peak emf per SPP losses.

In Fig 5.1(c), the reflectivity R, normalized to the reflectivity of the flat film, R_0, is plotted as a function of frequency for different modulation amplitudes at $\theta = 5°$ Each curve demonstrates two SPP resonance dips and an additional small peak around 2.15 eV related to the Rayleigh anomaly [57]. With an increase in the modulation amplitude, the resonance dips first become deeper and then broader.

Fig. 5.1(d) shows the spectral dependences of losses associated with the SPP excitation, P_{SPP}, which were calculated as the difference between the reflected intensity from a flat gold film ($h = 0$) and at the conditions of the SPP resonance for a particular h with the same θ and ω. At low h (10 and 20 nm), P_{SPP} decreases with increase in frequency, giving a small peak at ~2.15 eV. P_{SPP} is the highest at $h \approx 30\,\text{nm}$ for most of the spectrum, indicating the most efficient SPP excitation. With the further increase in h the spectral dependence $P_{SPP}(w)$ tends to, instead, increase with the increase of ω.

The plasmonic pressure force acting on an electron is determined by fields in a metal as

$$f_\alpha = \frac{1}{2} Re\left\{\chi\left(E_x \partial_\alpha E_x^* + E_y \partial_\alpha E_y^* + E_z \partial_\alpha E_z^*\right)\right\}. \tag{5.5}$$

The photoinduced emf is calculated by averaging the pressure force, f_{Lx} , over the volume of the metal film as [53]

$$\frac{U}{I} = \frac{1}{2\pi} \frac{\tau_{therm}}{\tau} \frac{L/I}{en_e} \frac{1}{h} \int_h \bar{f}_{L_x}(z) dz, \tag{5.6}$$

where I is the incident light intensity and L is the diameter of the illuminated spot.

The emf calculated in a flat film ($h = 0$), U_0, is pure photonic drag [58], which is small and plays a role only at the blue part of the spectrum. The plasmonic emf, $U - U_0$, calculated at $\tau_{therm} = 270$ fs, $L = 2$ mm, and $\theta = 5°$ is plotted in Fig. 5.1(e). The polarities of $U - U_0$ at the red and blue parts of the spectrum are opposite to each other, in each case corresponding to the drift of electrons in the direction of SPP propagation. The emf peaks change with variation of h in a similar way to the dips in reflectivity (Fig. 5.1(c)).

The ratio of the peak emf and maximum losses at SPR are plotted in Fig. 5.1(f) for the whole optical range. The curves are almost flat, corresponding to $C = \frac{1}{I}\frac{U-U_0}{R_0-R} = 2.2 - 2.5$ mV/(MW cm^2) at small modulation amplitudes, increasing to ~ 3-3.5 with an increase in h. They are negative at the red part of the spectrum, and positive at the blue, corresponding to backward or forward plasmon drag. The polarity switches at ~ 2.15 eV where the standing SPP wave is excited, providing zero momentum to electrons. Near the switching point the curves with high h demonstrate a small peak.

The flatness of the curves indicates that the momentum transfer from plasmons to electrons is directly proportional to the energy transfer, which correlates well with the conclusions of the theory [53] predicting a direct proportionality between the plasmon induced emf and absorption at relatively small modulations of the metal surfaces ($h \ll d$) and laminar electron flow. According to the results of the simulations, it holds up to amplitudes of 40–50 nm for our periodicity. In comparison with the experiment, the calculations correctly predict the magnitude, polarity and angular position of the PLDE peak observed experimentally in the gold film with

$h \sim 25$ nm see, figure 3 in [53]). However, the presence of additional contributions (clearly seen at large incidence angles) have yet to be taken into account.

In conclusion, the PLDE in a thin gold film with a sine-wave profile was analyzed theoretically for various amplitudes of the surface modulations in a broad optical range. The numerical simulations based on modified electromagnetic momentum loss approach was shown to provide adequate description of the emf associated with propagating SPPs at small amplitudes of surface modulations.

Plasmons in Sine Wave Films Vs Square Nanowires

Periodic arrays of plasmonic elements, such as 1 D arrays of metal strips can support propagating modes of plasmonic excitations [59, 60] which have a certain similarity with surface plasmon polaritons (SPPs) excited at dielectric-metal interfaces in continuous metal films. Discontinuous plasmonic systems may be advantageous for a number of applications due to a lower relative concentration of metal and, possibly, a lower loss. In order to better understand optical and plasmonic properties of periodic arrays of plasmonic strips of subwavelength periodicity, we study these systems theoretically. Experimental studies were conducte at Norfolk State University [61], in comparison with continuous metal gratings with a sine-wave modulated profile.

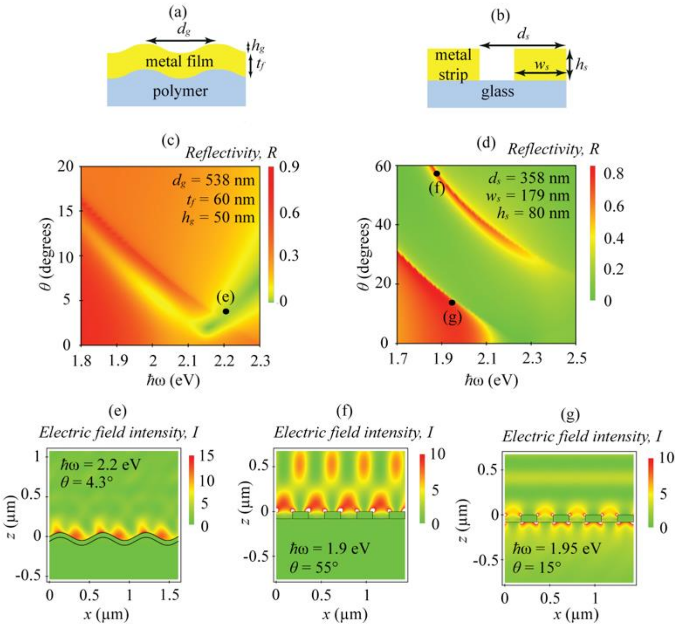

Fig. 5.2: Schematic cross-sections of the continuous sine-wave grating (a) and strips array (b); Zero-order reflectivity (shown with color) as the function of the angle of incidence, θ, and photon energy in the continuous grating (c) and strip array (d); Electric fields at resonance conditions in the continuous grating (e) and strip array (f, g). Parameters used in calculations are indicated.

The schematics of the structures under consideration and results of the numerical simulations are shown in Fig. 5.2. The two methods described in earlier chapters were used. The parameters used in the calculations correspond to those of my collaborator's experimental samples.

The continuous grating (Fig. 5.2(a)) supports SPPs at the metal-air interface at $\boldsymbol{k}_{spp} = n\boldsymbol{G} + \boldsymbol{k}_x$, where $\boldsymbol{k}_x$ is the projection of the optical k-vector, k_0, on the sample plane, $G = 2\pi/d_g$ and $n = \pm 1$ for our parameters. According to the simulations, the ratio $\xi = k_{spp}/k_0$ is very close to what is expected in flat films, $\xi = [(\varepsilon_m \varepsilon_d)/(\varepsilon_m + \varepsilon_d)]^{1/2}$, where ε_m and ε_d are the permittivities of metal and dielectric respectively. The solutions for the strip array (Fig. 5.2(b)) predict two different branches of collective excitations; one corresponds to the participation of the air-gold interface, and the other involves the glass-gold interface. The major difference between continuous and discontinuous systems is expected in the reflection at the resonance conditions: a dip in the zero-order reflectivity is expected in the continuous film while a peak in the zero-order reflectivity is expected for the strip array. Increased reflection is also predicted at $k_0 = 2\pi/d_g - k_0 \sin\theta$ (bright Rayleigh-Wood anomaly [62]).

In the experiment by Dr. Noginova's group at Norfolk State University, arrays of gold strips on glass substrates were fabricated using the interferometric lithography technique [63] first to form a photoresist pattern in SU-8 on top of a metal film and then transferring the pattern into the metal with a reactive ion etching, a dry etch. Gold continuous gratings were fabricated with forming a photoresist pattern on glass and subsequent deposition of metal onto the pattern.

In the reflectance measurements, the structure under study was mounted on the double goniometer stage, and illuminated with He-Ne laser at λ = 632.8 nm at p polarization (Fig. 5.3 (a)). The intensity of the reflected beam (zero order reflectivity) was measured as the function of angles of incidence, θ, and strips/grooves orientation, ϕ. A dip in the reflected intensity was observed in the continuous film (Fig. 5.3 (b)), while the strip array demonstrated a peak with an additional extra-sharp feature (Fig. 5.3 (c)) of angular width as small as ~ 0.04°. Changing the relative orientation of the strips (varying ϕ), the peak positions shifted toward larger θ.

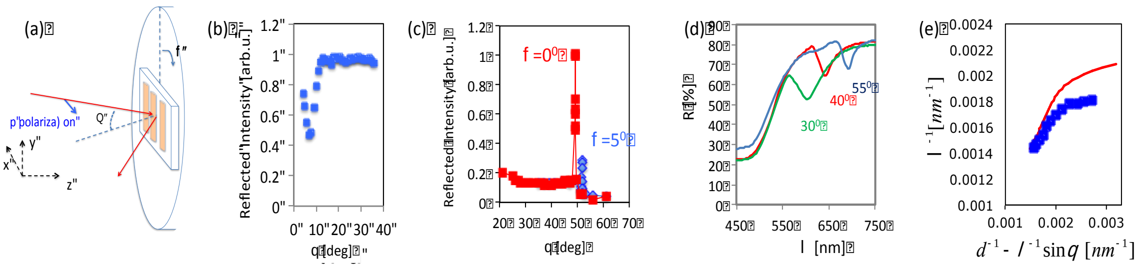

Fig. 5.3. (a) Setup in reflection measurements; (b, c) Reflected intensity in the sine-wave continuous film (b) and strip array (c); (d) reflection spectra at different θ as indicated; (e) the dispersion curve obtained from the reflection data (points). Solid trace is calculations for the continuous air-gold interface.

In the spectral measurements, the total reflected and transmitted intensities were recorded using the integrating sphere in the spectrophotometer setup. The reflection spectrum showed a dip as a characteristic signature of the resonance mode (Fig. 5.3(d)). The dispersion curve of this mode (Fig. 5.3 (e), points) derived from these measurements has a typical SPP character, but differs in magnitude from that of a continuous gold film, corresponding to slower propagation of the SPP in the discontinuous system.

Comparison of theoretical predictions and experimental data shows a very good agreement for both types of systems.

Conclusions

Throughout this thesis I have described multiple methods for semi-analytically solving Maxwell’s equations in complicated two dimensional structures. These methods were then used in a variety of ways to manipulate light. Rotating its polarization in a fraction the distance of any other proposed waveplate; potentially acting as an efficient coupling mechanism between optics and electronics; and having a plasmonic peak so strong and sharp that it holds incredible promise as a sensor.

We first modeled a metal-dielectric 1D optical meta-crystal. Then we used that to model arbitrary rectangular grating structures using a novel geometric series based approach. we then used this method to exactly model a metamaterial layer calculations performed by D. Keene et. al. By modifying the thickness and metal fraction, frequencies of polarization rotation could be moved almost anywhere within the optical range.

We also implemented Chandezon’s method, manipulating the metric in which Maxwell’s wave equations were to be solved, and beating the Rayleigh hypothesis’s limitations. Then we used the plasmonic pressure mechanism to find the forces on electrons and characterize the optoelectronic responses for various heights of sine wave metal structures, which may one day be used to couple electronic and optical computational devices.

We then used both methods together, comparing their reflectivity responses and theoretically explaining interesting details in the data of experiments done by Dr. Noginova’s group at Norfolk State University.

My work described in this thesis has the potential to push science quite far. Not just here at Georgia Southern University, where I have created a suite of computational wave optics programs useable in the search for more and more interesting surface properties. But also at large, where I have proposed a fair few realizable ideas for surface structures that could pave the way for new sensors, wave plates, maybe even realistic optical computers.

References

1. Wriedt, T., *Mie theory: a review*, in *The Mie Theory*. 2012, Springer. p. 53-71.
2. Bohm, D. and D. Pines, *A Collective Description of Electron Interactions. I. Magnetic Interactions.* Physical Review, 1951. **82**(5): p. 625-634.
3. Bohm, D. and D. Pines, *A Collective Description of Electron Interactions: III. Coulomb Interactions in a Degenerate Electron Gas.* Physical Review, 1953. **92**(3): p. 609-625.
4. Pines, D., *A Collective Description of Electron Interactions: IV. Electron Interaction in Metals.* Physical Review, 1953. **92**(3): p. 626-636.
5. Pines, D. and D. Bohm, *A collective description of electron interactions: II. Collective vs individual particle aspects of the interactions.* Physical Review, 1952. **85**(2): p. 338.
6. Ritchie, R.H., *Plasma Losses by Fast Electrons in Thin Films.* Physical Review, 1957. **106**(5): p. 874-881.
7. Otto, A., *Excitation of nonradiative surface plasma waves in silver by the method of frustrated total reflection.* Zeitschrift für Physik, 1968. **216**(4): p. 398-410.
8. Kretschmann, E., *Die bestimmung optischer konstanten von metallen durch anregung von oberflächenplasmaschwingungen.* Zeitschrift für Physik A Hadrons and Nuclei, 1971. **241**(4): p. 313-324.
9. Lvovsky, A.I., *Fresnel Equations*, in *Encyclopedia of Optical Engineering*. 2013, Taylor and Francis: New York. p. 1-6.
10. Airy, G.B., *On the diffraction of an object-glass with circular aperture.* Transactions of the Cambridge Philosophical Society, 1835. **5**: p. 283.
11. Rayleigh, L., *On the dynamical theory of gratings.* Proceedings of the Royal Society of London. Series A, Containing Papers of a Mathematical and Physical Character, 1907. **79**(532): p. 399-416.
12. Van den Berg, P. and J. Fokkema, *The Rayleigh hypothesis in the theory of reflection by a grating.* JOSA, 1979. **69**(1): p. 27-31.
13. Millar, R., *The Rayleigh hypothesis and a related least-squares solution to scattering problems for periodic surfaces and other scatterers.* Radio Science, 1973. **8**(8-9): p. 785-796.
14. Millar, R. *On the Rayleigh assumption in scattering by a periodic surface.* in *Mathematical Proceedings of the Cambridge Philosophical Society*. 1969. Cambridge Univ Press.
15. Chandezon, J., G. Raoult, and D. Maystre, *A new theoretical method for diffraction gratings and its numerical application.* Journal of Optics, 1980. **11**(4): p. 235.
16. Ko, D.Y.K. and J. Sambles, *Scattering matrix method for propagation of radiation in stratified media: attenuated total reflection studies of liquid crystals.* JOSA A, 1988. **5**(11): p. 1863-1866.
17. Cotter, N., T. Preist, and J. Sambles, *Scattering-matrix approach to multilayer diffraction.* JOSA A, 1995. **12**(5): p. 1097-1103.
18. Veselago, V.G., *The electrodynamics of substances with simultaneously negative values of and?* Soviet physics uspekhi, 1968. **10**(4): p. 509.
19. Pendry, J.B., *Negative refraction makes a perfect lens.* Physical review letters, 2000. **85**(18): p. 3966.

20. Schurig, D., et al., *Metamaterial electromagnetic cloak at microwave frequencies.* Science, 2006. **314**(5801): p. 977-980.
21. Yu, N., et al., *Light propagation with phase discontinuities: generalized laws of reflection and refraction.* science, 2011. **334**(6054): p. 333-337.
22. Keene, D. and M. Durach, *Hyperbolic resonances of metasurface cavities.* Optics express, 2015. **23**(14): p. 18577-18588.
23. Orlov, A., et al., *Complex band structure of nanostructured metal-dielectric metamaterials.* Optics express, 2013. **21**(2): p. 1593-1598.
24. Sturman, B., E. Podivilov, and M. Gorkunov, *Theory of extraordinary light transmission through arrays of subwavelength slits.* Physical Review B, 2008. **77**(7): p. 075106.
25. Sheng, P., R. Stepleman, and P. Sanda, *Exact eigenfunctions for square-wave gratings: Application to diffraction and surface-plasmon calculations.* Physical Review B, 1982. **26**(6): p. 2907.
26. Born, M. and E. Wolf, *Principles of optics: electromagnetic theory of propagation, interference and diffraction of light*. 1980: Elsevier.
27. Kildishev, A.V., A. Boltasseva, and V.M. Shalaev, *Planar photonics with metasurfaces.* Science, 2013. **339**(6125): p. 1232009.
28. Yu, N. and F. Capasso, *Flat optics with designer metasurfaces.* Nature materials, 2014. **13**(2): p. 139-150.
29. Zhao, Y., X.-X. Liu, and A. Alù, *Recent advances on optical metasurfaces.* Journal of Optics, 2014. **16**(12): p. 123001.
30. Hao, J., et al., *Optical metamaterial for polarization control.* Physical Review A, 2009. **80**(2): p. 023807.
31. Pors, A., M.G. Nielsen, and S.I. Bozhevolnyi, *Broadband plasmonic half-wave plates in reflection.* Optics letters, 2013. **38**(4): p. 513-515.
32. Pors, A. and S.I. Bozhevolnyi, *Plasmonic metasurfaces for efficient phase control in reflection.* Optics express, 2013. **21**(22): p. 27438-27451.
33. Jiang, Z.H., et al., *Broadband and wide field-of-view plasmonic metasurface-enabled waveplates.* Scientific reports, 2014. **4**: p. 7511.
34. Papakostas, A., et al., *Optical manifestations of planar chirality.* Physical Review Letters, 2003. **90**(10): p. 107404.
35. Drezet, A., C. Genet, and T.W. Ebbesen, *Miniature plasmonic wave plates.* Physical review letters, 2008. **101**(4): p. 043902.
36. Khoo, E.H., E.P. Li, and K.B. Crozier, *Plasmonic wave plate based on subwavelength nanoslits.* Optics letters, 2011. **36**(13): p. 2498-2500.
37. Zhao, Y. and A. Alù, *Manipulating light polarization with ultrathin plasmonic metasurfaces.* Physical Review B, 2011. **84**(20): p. 205428.
38. Ginzburg, P., et al., *Manipulating polarization of light with ultrathin epsilon-near-zero metamaterials.* Optics express, 2013. **21**(12): p. 14907-14917.
39. Slobozhanyuk, A.P., et al., *Purcell effect in hyperbolic metamaterial resonators.* Physical Review B, 2015. **92**(19): p. 195127.
40. La Porta, A. and M.D. Wang, *Optical torque wrench: angular trapping, rotation, and torque detection of quartz microparticles.* Physical review letters, 2004. **92**(19): p. 190801.
41. Johnson, P.B. and R.-W. Christy, *Optical constants of the noble metals.* Physical review B, 1972. **6**(12): p. 4370.

42. Elston, S., G. Bryan-Brown, and J. Sambles, *Polarization conversion from diffraction gratings.* Physical Review B, 1991. **44**(12): p. 6393.
43. Akbari, M., M. Onoda, and T. Ishihara, *Photo-induced voltage in nano-porous gold thin film.* Optics express, 2015. **23**(2): p. 823-832.
44. Durach, M., A. Rusina, and M.I. Stockman. *Giant surface plasmon induced drag effect (SPIDEr) in metal nanowires*. in *SPIE NanoScience+ Engineering*. 2009. International Society for Optics and Photonics.
45. Kurosawa, H. and T. Ishihara, *Surface plasmon drag effect in a dielectrically modulated metallic thin film.* Optics express, 2012. **20**(2): p. 1561-1574.
46. Kurosawa, H., et al., *Optical rectification effect due to surface plasmon polaritons at normal incidence in a nondiffraction regime.* Optics letters, 2012. **37**(14): p. 2793-2795.
47. Ni, X., et al. *Photon Spin Induced Collective Electron Motion on a Metasurface*. in *CLEO: QELS_Fundamental Science*. 2015. Optical Society of America.
48. Noginova, N., et al., *Plasmon drag effect in metal nanostructures.* New Journal of Physics, 2013. **15**(11): p. 113061.
49. Noginova, N., et al. *Controlling Plasmon Drag with Illumination and Surface Geometry*. in *CLEO: QELS_Fundamental Science*. 2015. Optical Society of America.
50. Noginova, N., et al., *Light-to-current and current-to-light coupling in plasmonic systems.* Physical Review B, 2011. **84**(3): p. 035447.
51. Vengurlekar, A.S. and T. Ishihara, *Surface plasmon enhanced photon drag in metal films.* Applied Physics Letters, 2005. **87**(9): p. 091118.
52. Kretschmann, E., *Decay of non radiative surface plasmons into light on rough silver films. Comparison of experimental and theoretical results.* Optics Communications, 1972. **6**(2): p. 185-187.
53. Durach, M. and N. Noginova, *On the nature of the plasmon drag effect.* Physical Review B, 2016. **93**(16): p. 161406.
54. Fann, W., et al., *Direct measurement of nonequilibrium electron-energy distributions in subpicosecond laser-heated gold films.* Physical review letters, 1992. **68**(18): p. 2834.
55. Sun, C.-K., et al., *Femtosecond-tunable measurement of electron thermalization in gold.* Physical Review B, 1994. **50**(20): p. 15337.
56. Raether, H., *Surface plasmons on smooth surfaces*. 1988: Springer.
57. Brevik, I., *Photon-drag experiment and the electromagnetic momentum in matter.* Physical Review B, 1986. **33**(2): p. 1058.
58. Maystre, D., *Theory of Wood's anomalies*, in *Plasmonics*. 2012, Springer. p. 39-83.
59. Marani, R., et al., *Plasmonic bandgaps in 1D arrays of slits on metal layers excited by out-of-plane sources.* International Journal of Optics, 2012. **2012**.
60. Søndergaard, T., et al., *Slow-plasmon resonant-nanostrip antennas: analysis and demonstration.* Physical Review B, 2008. **77**(11): p. 115420.
61. Mashhadi, S., et al., *Collective plasmonic oscillations in gold nanostrips arrays*. 2017.
62. Gao, H., et al., *Rayleigh anomaly-surface plasmon polariton resonances in palladium and gold subwavelength hole arrays.* Optics express, 2009. **17**(4): p. 2334-2340.
63. Fan, W., et al., *Large-area, infrared nanophotonic materials fabricated using interferometric lithography.* Journal of Vacuum Science & Technology B: Microelectronics and Nanometer Structures Processing, Measurement, and Phenomena, 2005. **23**(6): p. 2700-2704.